Progress in Neurobiology 229 (2023) 102501

Contents lists available at ScienceDirect

Progress in Neurobiology

journal homepage: www.elsevier.com/locate/pneurobio

Parallel neurodegenerative phenotypes in sporadic Parkinson's disease fibroblasts and midbrain dopamine neurons

MJ Corenblum [a], A. McRobbie-Johnson [b], E. Carruth [c], K. Bernard [b], M. Luo [d], LJ Mandarino [d], S. Peterson [e], MA Sans-Fuentes [e], D. Billheimer [e], T. Maley [b], ED Eggers [f], L. Madhavan [a,g,*]

[a] Department of Neurology, University of Arizona, Tucson, AZ, United States
[b] Physiological Sciences Graduate Program, University of Arizona, Tucson, AZ, United States
[c] Physiology Undergraduate Program, University of Arizona, Tucson, AZ, United States
[d] Department of Medicine, University of Arizona, Tucson, AZ, United States
[e] Statistical Consulting Lab, BIO5 Institute, University of Arizona, Tucson, AZ, United States
[f] Departments of Physiology and Biomedical Engineering, University of Arizona, Tucson, AZ, United States
[g] Evelyn F McKnight Brain Institute and BIO5 Institute, University of Arizona, Tucson, AZ, United States

ARTICLE INFO

Keywords:
Skin fibroblasts
Human Induced Pluripotent Stem Cells
Midbrain Dopamine Neurons
Aging
Parkinson's disease
Mitochondrial Dysfunction

ABSTRACT

Understanding the mechanisms causing Parkinson's disease (PD) is vital to the development of much needed early diagnostics and therapeutics for this debilitating condition. Here, we report cellular and molecular alterations in skin fibroblasts of late-onset sporadic PD subjects, that were recapitulated in matched induced pluripotent stem cell (iPSC)-derived midbrain dopamine (DA) neurons, reprogrammed from the same fibroblasts. Specific changes in growth, morphology, reactive oxygen species levels, mitochondrial function, and autophagy, were seen in both the PD fibroblasts and DA neurons, as compared to their respective controls. Additionally, significant alterations in alpha synuclein expression and electrical activity were also noted in the PD DA neurons. Interestingly, although the fibroblast and neuronal phenotypes were similar to each other, they differed in their nature and scale. Furthermore, statistical analysis revealed potential novel associations between various clinical measures of the PD subjects and the different fibroblast and neuronal data. In essence, these findings encapsulate spontaneous, in-tandem, disease-related phenotypes in both sporadic PD fibroblasts and iPSC-based DA neurons, from the same patient, and generates an innovative model to investigate PD mechanisms with a view towards rational disease stratification and precision treatments.

1. Introduction

Parkinson's disease (PD) is a relentlessly progressive neurodegenerative disorder characterized by incapacitating motor deficits and neurocognitive decline over the course of aging – but it has no cure (Bloem et al., 2021; Dorsey et al., 2018; Teves et al., 2017). Key to the discovery of effective therapeutics will be an improved understanding of the mechanisms underlying PD etiopathology, and the identification of biomarkers to diagnose the disease at early stages (Poewe et al., 2017; Tolosa et al., 2021). However, the lack of appropriate model systems that capture the complexity of human PD has hindered progress in this regard.

Although PD research has largely focused on the central nervous system, specifically on the loss of midbrain dopaminergic (DA) neurons and associated motor dysfunction, there has been an increasing recognition of the features of PD that are not related to nigrostriatal dopamine deficiency. In fact, PD has emerged as a multisystem disease with numerous clinical manifestations that relate to pathologic changes in widespread regions of both the central and peripheral nervous systems (Lim et al., 2009; Poewe, 2010; Shannon, 2007). These clinical features include many non-motor symptoms such as skin sensory and olfactory abnormalities, sleep disturbances, pain, and autonomic dysfunction, in addition to the classic motor symptoms. In terms of its development, PD is understood to originate from complex interactions between several genetic and environmental factors during aging (Poewe et al., 2017). Although these gene-environment interactions are not fully understood, studies have demonstrated that converging impairments in mitochondrial function, redox balance, and protein quality control are crucial

---

[*] Correspondence to: Department of Neurology, University of Arizona, 1501, N Campbell Ave, Tucson, AZ 85724, United States.
E-mail address: lmadhavan@arizona.edu (L. Madhavan).

https://doi.org/10.1016/j.pneurobio.2023.102501
Received 23 January 2023; Received in revised form 29 June 2023; Accepted 10 July 2023

processes mediating cellular death and dysfunction in PD (Johnson et al., 2019; Malkus et al., 2009).

In this study, we utilized human skin fibroblasts as well as iPSC-derived dopaminergic neurons (iPSC-DAN), as a two-tiered approach, to examine the cellular and molecular changes defining idiopathic PD. Skin fibroblasts are peripheral cells shown to be valuable in modeling PD as they can express growth, mitochondrial and metabolic alterations relevant to the disease (Carling et al., 2020; Galvagnion et al., 2022; Mortiboys et al., 2008; Teves et al., 2017). Importantly, these cells are known to maintain the age and epigenetic signatures of the patient, thus capturing the aging and environmental history, which are the biggest risk factors for PD (Auburger et al., 2012; Ivanov et al., 2016; Teves et al., 2017). In contrast, due to reprogramming, iPSCs are known to revert to a 'younger state' mostly devoid of aging markers (Aversano et al., 2022; Mertens et al., 2018). Thus, iPSCs and their neural progeny, such as DA neurons, may mainly convey mechanisms of early neural vulnerabilities in PD such as the influences of potential genetic variants. Together these two models reflect both early and age-relevant aspects of PD. They also synergistically present peripheral as well as more central (brain related) aspects of the disease. Thus, we propose that human skin fibroblasts and iPSC-derived neural cell types obtained from the same patient may provide a powerful means to investigate PD biology more holistically.

From this perspective, the current study assessed a range of processes including growth and morphology, redox status, mitochondrial structure and function, autophagy, alpha synuclein (aSyn) expression and neuronal electrophysiology in the human fibroblasts and iPSC-DAN. Basically, we found distinct changes that differentiated PD fibroblasts, from healthy age- and sex-matched controls. Moreover, these features were recapitulated in midbrain DA neurons, generated from the same fibroblasts, providing 'neural correlates' of the fibroblast changes. Interestingly, although several phenotypes in the fibroblasts and DA neurons mirrored each other, they also diverged with respect to their magnitude and precise characteristics. Intriguing associations between the cellular phenotypes and the patient's clinical features were also observed. Fundamentally, our study discovers spontaneous disease-related phenotypes expressed in concert in both sporadic PD patient fibroblasts and iPSC-DAN, generating a system amenable to study PD development and progression from both peripheral and central mechanistic perspectives.

2. Methods

2.1. Skin fibroblast and iPSC lines

Skin fibroblast and iPSC lines of idiopathic PD (no known gene mutations) and healthy control subjects were mainly obtained from the Parkinson's Progression Markers Initiative (PPMI) biorepository at Indiana University (supported by the Michael J. Fox Foundation and it corporate sponsors) with some lines from the Madhavan lab cell bank. All the chosen fibroblast lines were originally generated from upper arm skin biopsies collected under relevant Institutional Review Board approvals. 9 control (C1-C9; C1–6 from Madhavan lab, C7–9 from PPMI) and 8 PD (PD1–8 from PPMI) lines, which were age-matched, and contained 4–5 male and 4 female samples in each group from passages 4–5 were utilized for the study. The detailed clinical and demographic information related to these cell lines are described in Table 1. Induced pluripotent stem cells (iPSCs) derived from a subset of the fibroblast lines were also studied. Specifically, already generated and quality control checked iPSC lines from C1, C6, C8, C9, PD1, PD6, PD4 and PD8

Table 1
Demographics & Clinical Data.

Line ID	Group	Sex	Age at diagnosis (years)	Age at biopsy (years)	Disease Duration (years)	UPDRS3 (ON)	UPDRS TOT (ON)	UPDRS3	UPDRS TOT	Cog State	NPI-Cog	REM-Cat	A-Syn	PD Med Use
CON1	Control	M		75										
CON2	Control	M		80										
CON3	Control	M		74										
CON4	Control	M		59										
CON5	Control	F		66										
CON6	Control	F		68										
CON7	Control	F		59										
CON8	Control	F		61.5										
CON9	Control	M		44.5										
	Ratio F: M/ Mean	4:5		65.2										
PD1	PD	M	65.2	69.2	4	43	51	25	33	Normal	0-Normal	0-No RBD	471.5	2-DA Agonist
PD2	PD	M	68.8	71.3	2.5	26	55	35	64	Normal	1-Slight	1-RBD	2361.8	4-Ldopa + Other
PD3	PD	M	48.1	50.7	2.6	28	35	28	35	Normal	0-Normal	0-No RBD	998.1	3-Other
PD4	PD	M	75.5	77.8	2.3	21	46	27	52	Normal	1-Slight	0-No RBD	1313.2	1-Ldopa
PD5	PD	F	67.4	70.7	2.3	10	13	10	13	Normal	0-Normal	0-No RBD	972.1	0-Unmedicated
PD6	PD	F	61.6	64.5	2.9	12	30	11	25	Normal	0-Normal	0-No RBD	1313.6	2-DA Agonist
PD7	PD	F	81.8	84.8	3	15	27	15	27	Normal	0-Normal	1-RBD	1933.9	1-LDopa
PD8	PD	F	53.1	55.3	2.2	26	35	26	35	Normal	0-Normal	0-No RBD	804.5	3-Other
	Ratio F: M/ Mean	4:4	65.2	68	2.725	22.6	35.5	22	35.5					

NA, not available; UPDRS, Unified Parkinson's Disease Rating Scale Part 3 (on & off medications); UPDRS TOT, Unified Parkinson's Disease Rating Scale Total (on & off medications); Cog state; Diagnosis of cognitive state (1-normal, 2-MCI, 3-Dementia); NPI-Cog, Neuropsychiatric Inventory Score of Cognitive Impairment (0-Normal, 1-slight, 2-mild, 3-moderate, 4-severe); REM-Cat, REM Sleep Behavior Disorder Categorization (0-No RBD, 1-RBD); A-Syn, CSF alpha-synuclein levels; PD Medication Use, Medications taken by the patient for PD symptoms (0-unmedicated, 1-Ldopa, 2-DA agonist, 3-Other, 4-Ldopa + other, 5- DA agonist + other).

fibroblasts, from the same sources mentioned above, were used. The iPSC lines were age-matched and contained 2 male and 2 female lines in each group.

2.2. Cell culture

Fibroblasts: Fibroblasts were grown in Dulbecco's Modified Eagle's Medium (DMEM) (Thermofisher Scientific, Cambridge, MA), supplemented with 1X Non-Essential Amino Acid (NEAA) (Thermofisher Scientific, Cambridge, MA), 10% Fetal Bovine Serum (FBS) (Atlanta Biologicals, Flowery Branch, GA), and 1% Anti-mycotic Anti-biotic (Anti-Anti) (Gibco, Waltham, MA) at 5% CO$_2$ and 37 °C. Fibroblasts from passage 7–10 were used, and for all experiments, the passage numbers were kept consistent within groups to avoid cell replication related biases. Cells were plated and used for the different assays when they reached ~75% confluence in culture. All fibroblast lines were grown in parallel and assessed in at least triplicate for the experiments.

Induced pluripotent stem cells (iPSCs): iPSCs were maintained on Matrigel hESC-Qualified Matrix (Corning, Corning NY) in mTeSR Plus (Stemcell Technologies, Vancouver BC). Colonies were routinely clump passaged using enzyme-free Gentle Cell Dissociation Reagent (Stemcell Technologies). For

.

deriving midbrain DA neurons, a modified floor plate-based differentiation method involving dual SMAD inhibition was used (Chambers et al., 2009; Kriks et al., 2011). This method involves initiating the neural patterning of the iPSCs via inhibitors of the SMAD signaling pathway [LDN 193189 (100 nM, Tocris, Minneapolis MN), SB 431542 (10 µM, Tocris), and specification towards a ventral midbrain DA neuron fate using the morphogens sonic hedgehog (SHH C25II N-Terminus 100 ng/mL, R&D Systems, Minneapolis MN), Purmorphamine (2 µM, Tocris), and CHIR 99021 (3 µM, Tocris). This is followed by the stimulation of neuronal maturation through the application of ascorbic acid, brain derived neurotrophic factor (BDNF), glial cell-line derived neurotrophic factor (GDNF), Transforming growth factor type β3 (TGF-b3), DAPT, L-Ascorbic acid (AA), and cyclic AMP (cAMP) on Poly--L-Ornithine/Fibronectin/Laminin coated dishes [BDNF: 20 ng/mL, Peprotech, Cranberry NJ, GDNF: 20 ng/mL, Peprotech, TGF-b3: 1 ng/mL, Peprotech, DAPT: 10uM, Biogems, Westlake Village CA, AA: 200uM, Sigma-Aldrich, St. Louis MO, and cAMP: 0.5 mM, Sigma-Aldrich, Poly-L-Ornithine: mw30,000–70,000; 15 µg/mL, Sigma-Aldrich, Fibronectin: 4 µg/mL, Corning, Laminin: 6 ug/mL, Sigma]. Cells were assessed after 25 (dopaminergic progenitor stage) and 50–55 (more mature DA neurons) days of differentiation, when they were subjected to a variety of assays. All iPSC lines were differentiated in parallel and assessed in at least triplicate for all experiments. The schematic above gives a broad overview of the iPSC differentiation and characterization process. A more detailed methodology has been provided in the Supplementary Methods section.

2.3. Cell viability

Cellular viability was determined utilizing a MTT [3-(4,5-dimethylthiazol-2-yl)– 2,5-diphenyltetrazolium bromide] assay (Invitrogen, Waltham MA), as described previously (Kumar et al., 2018; Teves et al., 2017). Fibroblasts and iPSC-DAN were detached and processed into single cell suspensions and plated onto 96-well clear flat-bottom plates at 10,000 cells/well and 80,000 cells/well respectively (at least 4 replicates per experimental run). Cell negative and assay negative controls were also used. Briefly, cells were washed once with PBS and placed in phenol-free culture medium. Experimental wells and cell negative wells were then treated with 12 mM MTT (prepared as described in assay manual) at 37 °C for 2hrs. Assay negative wells received PBS only and were incubated in the same manner. A portion of the MTT solution was removed from each well and Dimethyl sulfoxide (DMSO; Sigma-Aldrich) added to solubilize the generated crystals. Absorbance was read on a standard plate reader (Tecan Infinite 200 Pro Plate Reader, Tecan, Zurich, Switzerland) at 540 nm.

2.4. Fibroblast growth and morphology

The growth and morphology of the fibroblasts were assessed when they reached 75% confluence (right before they are ready to be passaged) as described previously (Teves et al., 2017). Three variables pertaining to cellular growth were measured across 4 passages: (1) duration (in days) it took for the cells to reach 75% confluency; (2) total cell count at 75% confluency, and (3) population doubling time [PDT = 3.32 x [Log (number of cells at 75% confluence) – Log (number of cells plated) + number of cells/ cm^2].

For morphological analysis, the fibroblasts were plated at 40,000 cells/well on poly-D-lysine (0.1 mg/mL) coated glass coverslips in 24-well plates. The cells were fixed using 4% paraformaldehyde (PFA,

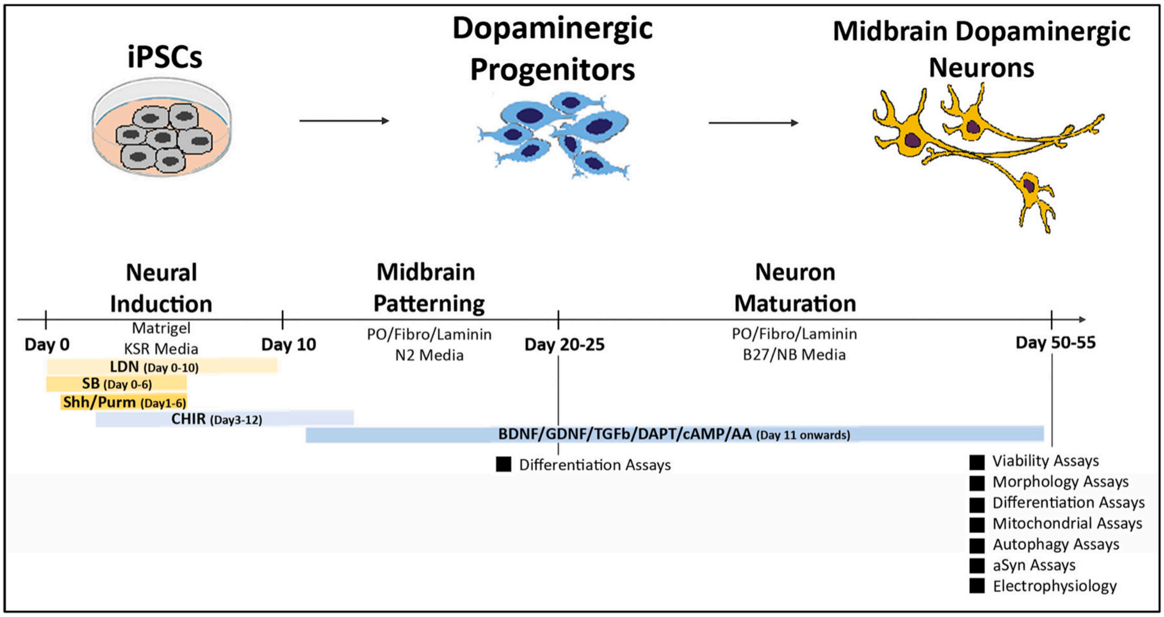

Electron Microscopy Sciences, Hatfield, PA) for 20 min at room temperature. After washing with 1X Phosphate-buffered saline (PBS: Thermofisher Scientific, Cambridge, MA), the fibroblasts were treated with 0.1% Triton-X-100 (Sigma-Aldrich, Darmstadt, Germany) in PBS for 5 min. Cells were then stained with 1.65uM Alexa Fluor 488 Phalloidin (Invitrogen, Waltham, MA) for 20 min at room temperature. Images were subsequently obtained from 6 random fields per coverslip using a Zeiss Axio Imager M2 Upright Fluorescent Microscope (Zeiss, Jenna, Germany). Images were taken at 40X with exposure conditions standardized across all cell lines. Afterwards, the single-channel images were processed in CellProfiler open-source software (Broad Institute at MIT, Cambridge, MA). An analysis pipeline was created to correctly identify individual nuclei and cell perimeter/outlines. Using this pipeline, several parameters of interest were analyzed including the density (neighbors), size (area and perimeter) and shape (form factor and eccentricity) of cells for all lines.

2.5. Immunocytochemistry

Fibroblasts were enzymatically dissociated at ~75% confluence and 20,000 cells plated on glass coverslips coated with 0.1 mg/mL Poly-D-Lysine (Sigma-Aldrich, Darmstadt, Germany) and placed in 24-well plates. iPSC-DAN were dissociated and replated on glass coverslips at 150,000 cells per coverslip or 100,000 cells per well of an 8-well chamber slide, both coated with Poly-L-Ornithine (15 ug/mL Sigma), Fibronectin (4 ug/mL Corning), Laminin (6 ug/mL Sigma). All cells were fixed for 20 min at room temperature (RT) with 4% PFA. For immunocytochemistry, cells were blocked for 2hrs at room temperature [in 2% normal goat serum, 1% Bovine Serum Albumin, 0.4% Triton-X-100 in PBS] and incubated in primary antibody overnight at 4 °C in a humidity chamber. Primary antibodies were detected in a 2-hour incubation at RT with secondary antibodies coupled to fluorochromes Alexa Fluor 488, 594, 647 (Life Technologies-Molecular Probes, Grand Island, NY) or a biotinylated secondary (Vector Laboratories, Newark CA) followed by a Streptavidin-tagged Alexa Fluor, and counterstained with 4',6'-diamidino-2-phenylindole, dihydrochloride (DAPI, Life Technologies). Control conditions constituted the deletion of the primary antibody or secondary antibody and the inclusion of relevant isotype specific antibodies and sera instead of the omitted antibodies. Primary antibodies used were as follows: ATPIF1 (1:350); Tuj1 (1:200); TH (1:2000); LMX1A (1:250); FoxA2 (1:200); Girk2 (1:1000); Map2 (1:8000); aSyn (1:400), pSyn (1:2000). More antibody details can be found in the table in the Supplementary Methods section.

2.6. Microscopy and cell counts

Fluorescence analysis was performed using a Zeiss LSM880 Inverted confocal microscope (Zeiss, Jena, Germany). Z sectioning was performed at 1–2 μm intervals in order to verify the co-localization of markers. Image extraction and analysis was conducted via the Zen Blue software. A Zeiss Axio-Imager M2 microscope connected to an Axiocam MRm digital camera and Microlucida software (v2019.1.3, MBF Bioscience) was used for epifluorescence microscopy. A Zeiss Axio Observer A1 inverted microscope with Axiocam MRc camera and AxioVision software was used for phase contrast microscopy. Quantitative analyses were conducted by a person blinded to the groups and lines.

Cell counts: For the TH and TH/Girk2 cell counts, 6 random fluorescence images/well were taken at 63X magnification of cells in 8-well chamber slides (duplicate wells/line), and the number of positively stained cells was elucidated and expressed as percent of Dapi (TH counts) or percent of TH (TH/Girk2 counts). TH, TH/FoxA2, Tuj1, Tuj1/LMX1A cell counts were imaged and quantified in the same manner and expressed as percent of Dapi (TH counts) or percent of TH (TH/FoxA2 counts) and percent of Dapi (Tuj1 counts) or percent of Tuj1 (Tuj1/LMX1A counts). For quantification of the aSyn mean intensity signal, 6 random fluorescence images/well were taken at 63X magnification of cells in 8-well chamber slides (duplicate wells/line) keeping the exposure and gain settings consistent among all lines and images. Individual images were loaded into Cell Profiler (Broad Institute) and a set pipeline was run which identified each cell's nucleus and quantified the intensity of its surrounding aSyn staining on a pixel-by-pixel basis. Additionally, the number of $aSyn^+$ cells of Dapi stained cells was also enumerated across 6 random fields/well under 63X magnification. For pSyn quantification, 6 random fluorescence images/well were taken at 63X magnification of cells in 8-well chamber slides (duplicate wells/line), and the number of positively stained cells was elucidated and expressed as percent of TH. Quantification of neuronal soma size and number of neurites was conducted using NIH Image J software. 6 randomly placed epifluorescence images/well were taken at 63X magnification of Map2 staining of cells in 8-well chamber slides (duplicate wells/line). Images were loaded into Image J and a freehand selection tool was utilized to precisely trace each cell's soma and the area was measured in square pixels and number of primary neurites was enumerated.

Mitochondrial network analysis: Confocal images were acquired of the ATPIF1 immunostaining using a 63X objective (3 coverslips and 15 images/line). Z-stacks were acquired at 0.38uM intervals and compressed to a 2D maximum intensity projection image using the ImageJ software (NIH, v1 53c).

Skeleton Analysis: From single channel images, a single cell was outlined, and the outside cleared such that only one cell remained per frame. Images were converted to binary, and total area was calculated using the measure feature. Morphological features were quantified using an objective and computer-aided skeleton analysis method previously described in detail (Young and Morrison, 2018). After thresholding, a series of ImageJ plugins were consistently applied across all images to ensure adequate visualization of cell process before the conversion to binary and skeletonized images. The skeletonized representations of original photomicrographs were used for data collection of morphology parameters using the AnalyzeSkeleton (2D/3D) plugin (Arganda-Carreras et al., 2010). These features were then divided by the total area of each cell, in order to normalize to the total size of each cell.

Fractal and Lacunarity Analysis: Single channel images were converted to binary, and then run through the ImageJ plugin, FracLac. For fractal analysis the program was set up so that NumG = 5. All binary images were run through the program using the batch feature. D_B, Lacunarity, and Density of Foreground Pixels were selected from the resulting data table.

2.7. Autophagy flux assays

To measure autophagic flux, confluent wells in a 6-well plate were incubated with 20 mM NH_4Cl (Sigma-Aldrich, St Louis MO) and 300 μM leupeptin (Sigma-Aldrich) for 4hrs in standard culture medium with serum or serum-free conditions before protein samples were collected as below and western blotting was performed (Teves et al., 2017).

2.8. Western Blotting

To isolate protein, fibroblasts and DA neurons were trypsinized, washed in PBS, and resuspended in RIPA buffer (Sigma-Aldrich, St. Louis MO) containing Protease Inhibitor Cocktail (Sigma-Aldrich). After 1 hr incubation in RIPA on ice, cells were sonicated and centrifuged at 4 °C for 30 min at 15,000 × *g*. The supernatant containing the soluble protein was removed, quantified by the Lowry method, and stored at − 20 °C. To detect LC3 and p62, samples from Control and PD fibroblasts, and DA neurons, were run on a 12% acrylamide gel and transferred to a PVDF membrane using a wet transfer system. For aSyn, protein samples were run on a 12.5% acrylamide gel and subsequently transferred to a PVDF membrane. For pSyn, protein samples were run on a 4–15% Gradient TGX gel (Bio-Rad, Hercules CA) and transferred to a PVDF membrane. After 1 hr of incubation with blocking solution [0.1 M tris buffered saline with 0.1% Tween-20 (TBS-T) with 5% bovine serum albumin (BSA, ThermoFisher Scientific, Waltham MA) or 5% dry milk], primary and secondary antibodies were applied. Specifically, membranes were incubated overnight in primary antibodies targeting LC3 (1:2000) and p62 (1:2000), aSyn (1:500) and pSyn (1:500) diluted in blocking solution with 0.1% Tween-20 (Sigma-Aldrich). The next day, after washing in 0.1 M TBS with 0.1% Tween-20, membranes were incubated in appropriate horseradish peroxidase secondary antibodies for 1 hr and developed using SuperSignal west Femto ECL substrate (ThermoFisher) and scanned on an Azure 500 (Azure Biosystems, Dublin CA). ImageJ software was utilized to select equal regions of interest across all bands and the measurements tool employed to gain relative intensity units. Each band was normalized to its corresponding loading control (Beta Actin) for that lane.

2.9. Transmission electron microscopy

Fibroblasts were plated at 1 × 10^6 cells per 10 mm petri dish and allowed to grow to confluence. iPSC-DAN were plated in 6-well plates and allowed to differentiate and mature to Day 50. The cells were fixed in-situ with 2.5% glutaraldehyde in 0.1 M piperazine-N,N'-bis (1-ethanesulfonic acid) (Glut-PIPES buffer) for 1 hr at room temperature, washed 3 times with 0.1 M PBS pH 7.4, and scraped off well bottoms. Then the cells were transferred to a 1.5 mL microcentrifuge tube and centrifuged at 1000 x g. Afterwards, the cell pellets were post-fixed with 1% osmium tetroxide in 0.1 M PBS for 30 min, resuspended and washed in the same buffer and in distilled/deionized water. Subsequently, the cell pellets were dehydrated through a series of ethanol and acetonitrile and infiltrated with 1:1 acetonitrile/ Spurr resin overnight. The next day pellets were embedded in 3 changes of Spurr resin 60 min each and allowed to polymerize in Beem embedding capsules for 36hrs at 60 °C. Thin sections (90 nm) were obtained on a RMC PowerTome XL 9 ultramicrotome onto uncoated 150 mesh copper grids and stained with 2% uranyl acetate and lead citrate. Images were acquired using a Tecnai G2 Spirit BioTwin transmission electron microscope (FEI, Hillsboro, OR USA) with a side mounted XR41 AMT 4 Mpix digital camera, operated at 100 kV. Morphometric measurements were conducted in digital images and the number of autophagic vacuoles or distorted mitochondria per cell profile (10–15 cell profiles) across a minimum of 10 micrographs per line were counted using standard criteria as described before (Anandhan et al., 2021; Teves et al., 2017).

2.10. Reactive oxygen species (ROS) measurements

ROS levels were assessed using the DCFDA/H2DCFDA Cellular ROS Assay Kit (Abcam, Waltham MA), as describe before (Oyama et al., 1994; Teves et al., 2017). Fibroblasts and iPSC-DAN were detached, processed into single cell suspensions, and plated onto 96-well black-walled flat-bottom plates at 10,000 cells/well and 80,000 cells/well, respectively, to include at least 4 replicates per experimental run. During the assay, following manufacturer's instructions, culture media was removed and 25uM DCFDA solution was added. Cell negative and assay negative controls were also used. Cells were incubated for 45 min at 37 °C in DCFDA solution, after which they were washed in PBS, and fluorescence measured at 485Ex/535Em on a standard plate reader (Tecan Infinite 200 Pro Plate Reader, Tecan, Zurich, Switzerland). Values were normalized to total protein expression using a standard Bradford assay.

2.11. Seahorse mito stress test

Mitochondrial function was probed utilizing a Seahorse XF Cell Mito Stress Test kit (Agilent Technologies, Santa Clara CA) (Teves et al., 2017). Fibroblasts were plated in a Seahorse XFe96 V3 PS plate at least 8 replicates per experimental run at an optimized seeding density of 20,000 cells per well. iPSC-DAN were plated in a Seahorse XF24 V7 PS plate at least 5 replicates per line at an optimized seeding density of 100,000 cells per well. Cells were cultured under standard 5% CO_2 and 37 °C conditions. Seahorse XF base medium enriched with 10 mM glucose, 2 mM L-glutamine and 1 mM sodium pyruvate was equilibrated to 37 °C with an adjusted pH of 7.35 ± 0.05. All wells were carefully washed 3 times with the Seahorse XF base medium and then incubated for 1 hr in assay media in a 37 °C CO_2-free incubator before the Mito Stress test was conducted. Successive administration of Oligomycin (Oligo), Carbonyl cyanide p-trifluoro-methoxyphenyl hydrazone (FCCP), and Rotenone/Antimycin (R/A), all modulators of respiration, were performed in the Seahorse XF Flux Analyzer (Fibroblasts: 1 μM Oligo, 2 μM FCCP, 1 μM/1 μM R/A. DA neurons: 1 μM Oligo, 1 μM FCCP, 2 μM/2μM R/A). Values were normalized to total protein concentration via a standard Bradford assay.

2.12. Electrophysiology assays

iPSC-DAN were plated on individual glass cover slips and kept in culture media at 37 °C until the time of experiments. Cells were removed from culture media and immediately used for recording. Extracellular solution used for whole cell recordings was kept at room temperature and contained the following (in mM): 125 NaCl, 2.5 KCl, 1.00 $MgCl_2$, 1.25 NaH_2PO_4, 20 glucose, 26 $NaHCO_3$, and 2 $CaCl_2$. The intracellular solution in the recording pipette contained the following (in mM): 120 K D-Gluconate, 25 KCl, 10 HEPES, 10 EGTA, 4 phosphocreatine-Na2, 4Mg-ATP, 2 Na-GTP, 1 $CaCl_2$, and 0.1% sulforhodamine-B dissolved in water and was adjusted to pH 7.2 with CsOH.

Electrodes were pulled from borosilicate glass (World Precision Instruments, Sarasota, FL) using a P97 Flaming/Brown puller (Sutter Instruments, Novato, CA) and had resistances of 5–8 MΩ. Liquid junction potentials of 20 mV, calculated with Clampex software (Molecular Devices, Sunnyvale, CA), were corrected before recording. Spontaneous events were sampled at 10 kHz and filtered at 6 kHz with the four-pole Bessel filter on a MultiClamp 700B patch-clamp amplifier (Molecular Devices) before being digitized with a Digidata 1140 data acquisition system (Molecular Devices) and Clampex software.

iPSC-DAN were considered spontaneously active if they spiked at least once without current steps. Cells were considered inducibly active if they elicited spikes after or during a − 30pA or + 30pA current step. Non-active cells never exhibited meaningful changes in membrane voltage. Spontaneous cell frequency, peak amplitude, decay tau, inter-event interval, and time to peak were analyzed using Molecular Devices Clampfit threshold search event detector software. Means were analyzed using Sigmaplot software to compute ANOVA SNK post-hoc test. Differences were considered significant when $p \leq 0.05$. Membrane capacitance was measured at the time of recording.

2.13. Statistical analysis

GraphPad Prism 9 software (San Diego, CA) was used for statistical analyses for data in Figs. 1–7 and supplementary figures. For comparing two groups, unpaired *t* tests were used. For comparisons between three or more groups, one-way analysis of variance (ANOVA) followed by Tukey's or Bonferroni's post-hoc test for multiple comparisons between treatment groups was conducted. When there were two independent variables involved, a two-way ANOVA test with Tukey's multiple comparisons was used. For the ATPIF1 image analysis, to assess the morphological differences between groups while also capturing the variability between cells within the same line, each cell was representative of itself, and images were not averaged across lines. For the western blot analysis of autophagy markers (Figs. 3 and 7) a repeated measures ANOVA with post-hoc Tukey or Sidak's multiple comparison tests was applied. For the electrophysiology data, a Fisher's exact test (Fig. 8B), one-way ANOVA or two-way ANOVA tests with Student-Newman-Keuls posthoc test (Fig. 8C-D) were used. In all cases, differences were accepted as significant at $p < 0.05$.

For the statistical correlation data (Figs. 9 and 10) analysis was

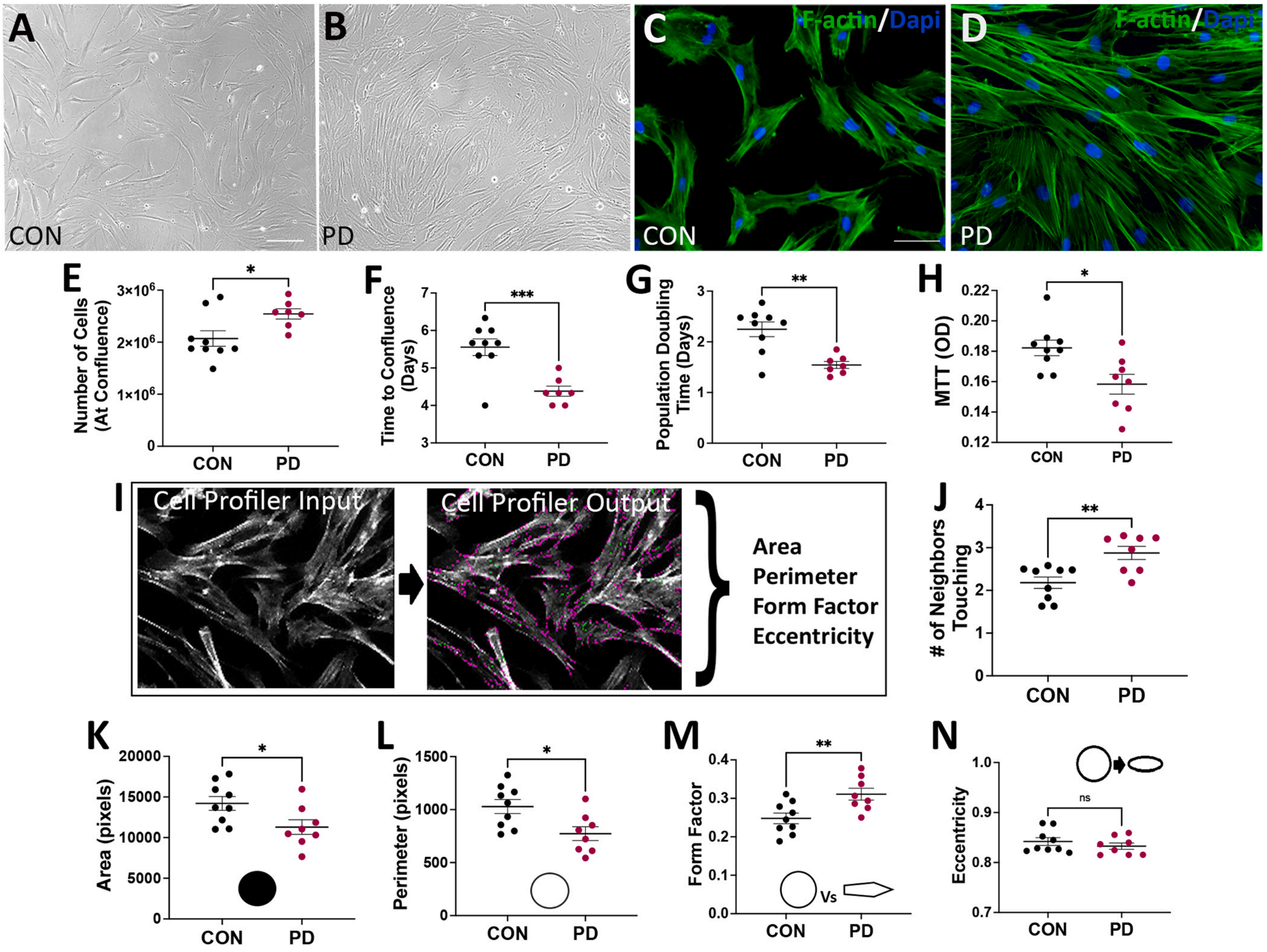

Fig. 1. : Growth dynamics and morphological properties of the patient-derived fibroblasts. CON and PD fibroblasts exhibited perceptible differences in their spatial growth patterns as depicted in the phase images in (A-B). Staining the cells with Phalloidin (fluorescent tag that binds to F-Actin) allowed to clearly visualize these growth differences and enabled a careful assessment of their morphological properties via NIH Cell Profiler (C, D, I). (H) shows data comparing the cellular viability of PD vs CON fibroblasts using an MTT assay. Comparisons between the number of live cells at 75% confluence, the time taken to reach 75% confluence and the population doubling time are in (E-G). The number of cellular neighbors is shown in (J). Results from shape and size assessments, specifically area (K), perimeter (L), form factor (M), and eccentricity (N), between CON and PD fibroblasts are in (K-N). Scale Bars: (A-B) = 200 µm, (C-D) = 100 µM. $^{*}p < 0.05$, $^{**}p < 0.01$; Mean ± SEM, Unpaired t-tests, n = 8–9 independent lines/group.

performed using R statistical software (V4.1.2; R Core Team 2021). Plots were generated using ‘ggplot2’ package (v3.4.2; Wickham, 2016). Correlation plots were obtained using ‘corrplot’ package (v 0.92; Wei and Simko 2021). To evaluate the magnitude and direction of the change for the graphs in Fig. 9, for each assay, separate regression lines were fitted for Neurons and Fibroblasts. The slope of these lines indicates the difference between PD and CON means. To test the hypothesis of a difference in slope between fibroblasts and neurons, we used Welch-Satterthwaite two-sample t-test (Welch, 1947; Satterthwaite, 1946), which is appropriate groups when the variances of the slopes are unequal. To investigate the potential association between pairs of variables of interest, correlation matrices were constructed using the Pearson correlation coefficient. This coefficient measures the linear relationship between two continuous variables and ranges from -1 to $+1$, with values close to $+1$ indicating a strong positive correlation, values close to -1 indicating a strong negative correlation, and values close to 0 indicating no correlation. A two-tailed test was conducted to assess if each correlation coefficient differed from zero (Kutner et al., 2004). The results of the correlation matrix were presented graphically using a heat map, with the direction and strength of the correlation indicated by the color and intensity of the cell, respectively. Moreover, Pearson coefficients between each pair of variables in the dataset of interest are also indicated. In all cases, differences were accepted as significant at $p < 0.05$. The exact sample size and specific statistical details of each experiment of the study are also provided within the relevant result and legend sections.

3. Results

3.1. PD and Control fibroblasts show different growth patterns and morphology

Several fibroblast lines from sporadic PD subjects and age- and sex-matched healthy control individuals were studied. The details of the cell lines and the associated clinical and demographic information is displayed in Table 1. First, the growth and morphological characteristics of fibroblasts were examined. All assessments were conducted right before passage when the cells had reached ~75% confluence in culture. At this stage, cells within control cultures were observed to be large, well ramified, and evenly distributed over the culture surface, as typical of mature fibroblasts. PD fibroblasts on other hand were smaller and more spindle shaped. Additionally, the PD cultures were generally denser and

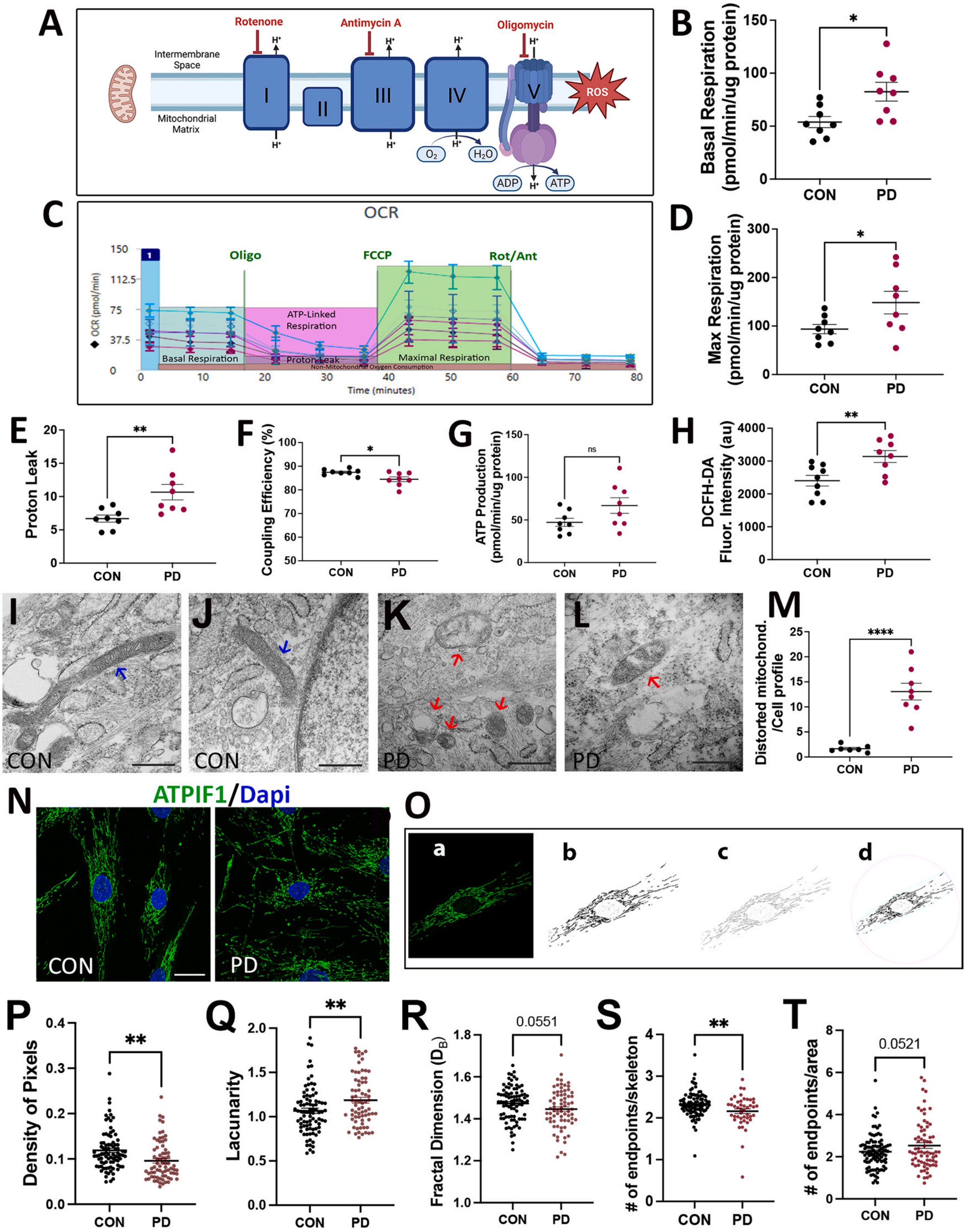

Fig. 2. : Mitochondrial-linked function analysis of the fibroblasts. (A) Schematic depiction of the mitochondrial electron transport chain and the 3 major inhibitors applied via the Seahorse assay to probe mitochondrial respiratory function. (C) shows example traces from the Seahorse Mito Stress test and some of the main parameters measured. (B-G) show results comparing the different mitochondrial function outputs obtained, particularly, basal respiration (B), maximal respiration (D), proton leak (E), coupling efficiency (F), and ATP production (G). Results from a DCFH-DA assay, showing differences in the production of gross ROS levels between CON and PD fibroblasts is in (H). TEM images showing typical mitochondria seen in CON (I, J; red arrows point to long tubular mitochondria) and PD (K, L; blue arrows point to smaller, swollen distorted mitochondria) cultures. Quantification of distorted mitochondria in CON and PD cells is shown in (M). Mitochondria were tagged via anti-ATPIF1 immunostaining (N), and an Image J pipeline was applied to threshold and skeletonize the ATPIF1 epifluorescence images allowing for characterization of mitochondrial networks (O). The major steps in the pipeline involved (a) single cell is isolated in image j, (b) image is converted to binary image, (c) binary image is skeletonized for the skeleton analysis resulting in the branch length and endpoints measurements, and (d) binary Image is run through fraclac which gives the lacunarity and pixel density. Mitochondrial properties were assessed by estimating the density of pixels (P), lacunarity (Q), fractal dimension (R), and number of endpoints (S, T). Scale Bars: (I-L) = 500 nm, (N) = μm. *$p < 0.05$, * *$p < 0.01$; Mean ± SEM, Unpaired t-tests, n = 8–9 independent lines/group. Data from the ATPIF1 mitochondrial network analysis is presented from 72 to 95 individual fibroblasts across 8–9 PD and CON lines to account for cell-cell variability in addition to line differences.

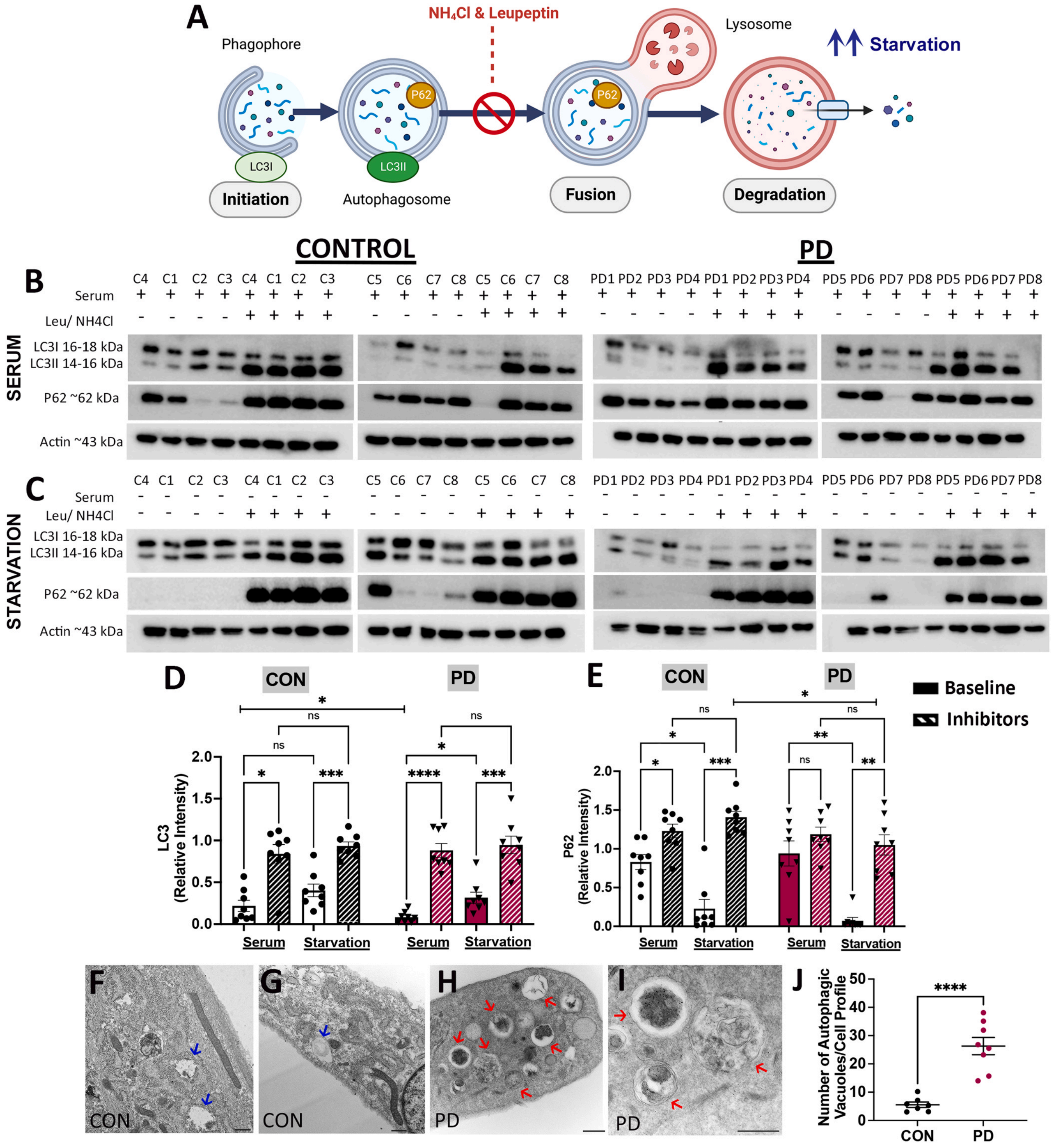

Fig. 3. : Autophagic alterations in PD fibroblasts. A schematic depicting the main phases of the macroautophagy pathway, and its classic activators and inhibitors, is in (A). Expression of the standard autophagy markers, LC3 and p62, were studied under baseline (B: serum present) and starvation (C: serum absent) conditions, with or without the lysosomal inhibitors NH4Cl/Leup, via western blotting. Densitometric quantification of the blots is shown in (D, E). No other comparisons, besides the ones annotated in the graphs, showed statistically significant differences between PD and Control groups. Overall two-way RM ANOVA analysis indicated that the effect of treatment was highly significant in relation to LC3 ($P < 0.0001$, $F_{3,\ 42} = 55.19$) and P62 ($P < 0.0001$, $F_{3,\ 42} = 53.55$), and no significant interaction between group (C and PD) and treatment (+/- inhibitors and +/- serum). (F-I) contains representative TEM images comparing the presence of autophagic structures (autophagosomes and autolysosomes) in CON (F, G; blue arrows point to autophagic vesicles) vs PD (H, I; red arrows point to several autophagic vesicles with varied cargoes) cells, and the associated quantification is in (J). Scale Bars: (H-L) = 500 nm. $*p < 0.05$, $* *p < 0.01$, $* **p < 0.001$; Mean + SEM, two-way RM ANOVA with Tukey's multiple comparison test in (D, E), and Unpaired t-tests in (J). n = 7–8 independent lines/group.

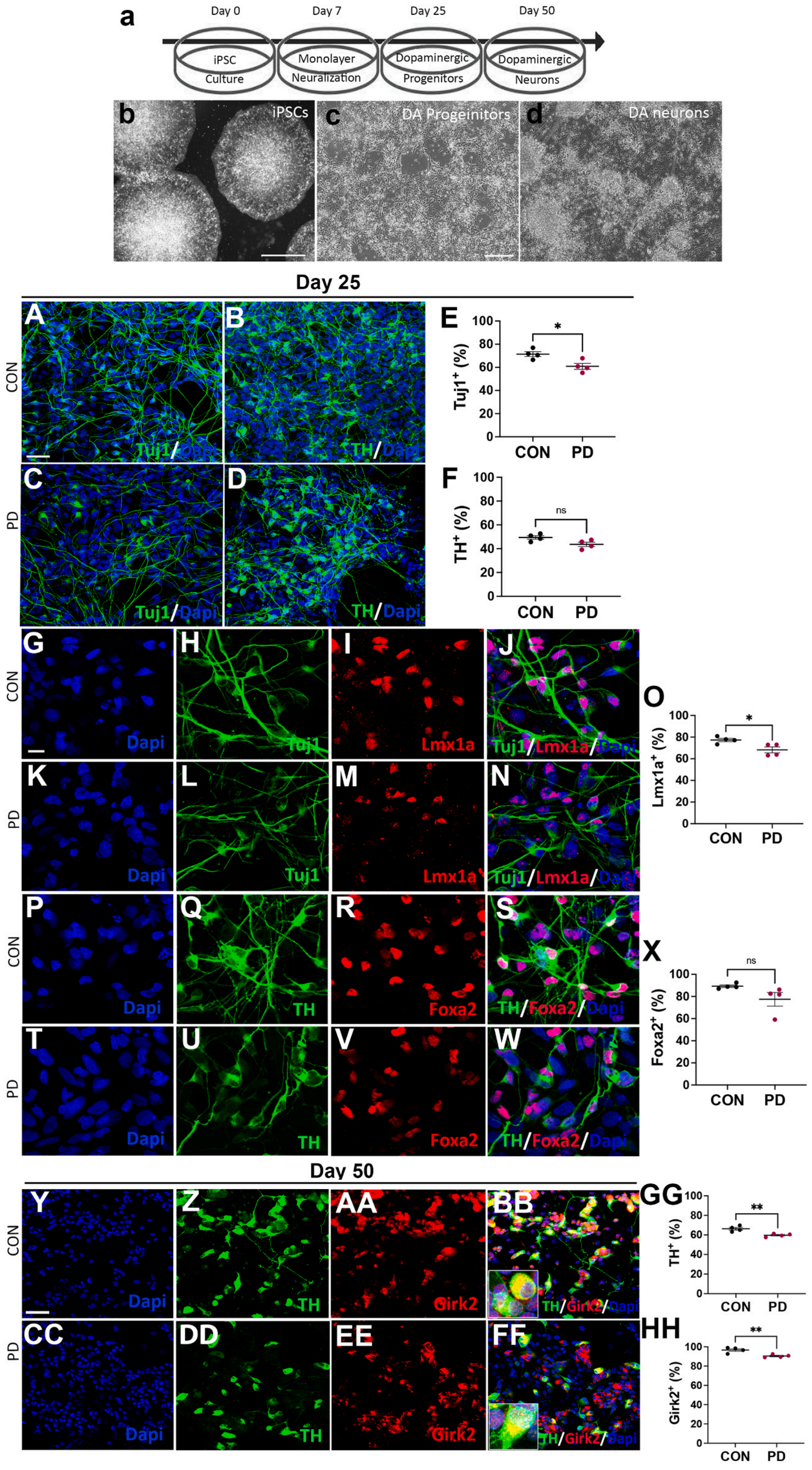

Fig. 4. : Generation and characterization of matched iPSC-DAN lines from the patient fibroblasts. Using a modified dual-SMAD inhibition protocol, iPSCs were differentiated and matured into midbrain DA neurons (a). Phase contrast images are depicted at initiation of differentiation (b – iPSC colonies), DA progenitor stage (c – Day 25) and maturing DA neurons (d – Day 50). CON and PD cells were immunostained with the neuronal marker, Tuj1 (A, C), and midbrain DA neuron marker, TH (B, D) at Day 25. Quantification of the efficiency of Tuj1$^+$ and TH$^+$ neuron production is shown in (E, F). Expression of the standard midbrain neuron markers Lmx1a (% of Tuj1$^+$ cells) and Foxa2 (% of TH$^+$ cells) was also assessed at this stage (G-W, O, X). At day 50, TH/Girk2 co-expression was examined to determine mature A9-type midbrain DA neuron generation efficiency (Y-FF, GG, HH). High magnification views of the TH/Girk2 double-positive cells are in the insets in (BB) and (FF). Scale Bars: (b) = 1000 μm, (c-d) = 100 μm, (A-D, G-W, Y-FF) = 20 μm. $*p < 0.05$, $**p < 0.01$; Mean ± SEM, Unpaired t-tests, n = 4 independent lines/group.

contained closely packed cells aligned along their longitudinal axis (Fig. 1**A, B** - phase contrast images; Fig. 1**C, D** - high magnification fluorescent images of Phalloidin/DAPI stained cells, Phalloidin binds to F-Actin).

To further investigate these observations, we quantified the total number of cells in the culture flasks at 75% confluence and assessed their growth rate. It was found that there were significantly higher numbers of cells in the PD flasks (Fig. 1**E**; p = 0.0266, Unpaired t-test, t = 2.478, df=14), and the time taken to reach 75% confluence was shorter with the PD cultures (~4.5 days) compared to controls (~5.5 days) (Fig. 1**F**; p = 0.0009, Unpaired t-test, t = 4.197, df=14). Further analysis indicated that the population doubling time (PDT) of control fibroblasts was indeed significantly longer than that of PD cells (Fig. 1**G**; p = 0.0014, Unpaired t-test, t = 3.970, df=14). Furthermore, PD cultures were found to be denser, with each cell surrounded by more neighboring cells, than controls (Fig. 1**J**; p = 0.0036, Unpaired t-test, t = 3.495, df=15). Interestingly, although more cells were detected in the PD cultures, it was also determined that PD cells had lower viability rates than control

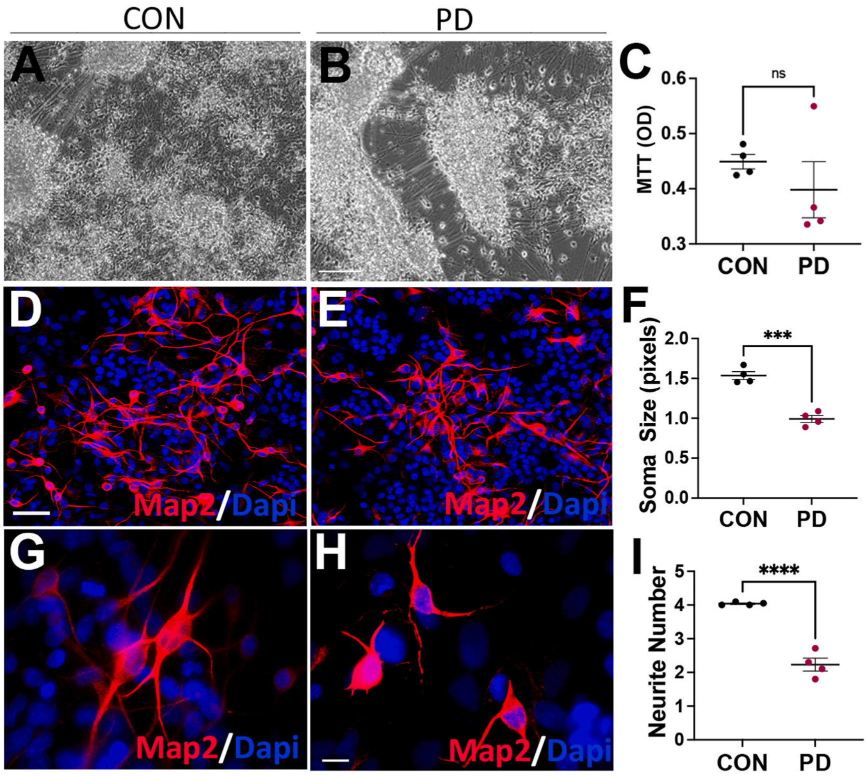

Fig. 5. : Assessment of the viability and morphological features of matched iPSC-DAN. Comparative phase images of CON and PD fibroblast-based iPSC-DAN, at Day 50 post-differentiation, is displayed in (A, B). Results from a MTT assay comparing the viability of CON vs PD iPSC-DAN is in (C). Morphological assessment was conducted on Map2 immunostained cells (D-E, G-H show higher magnification views). In particular, the soma size (F) and the number of neurites/cell (I) were estimated via Image J. Scale Bars: (A-B) = 100 µm, (D-E, G-H) = 20 µm. *p < 0.001 * **p < 0.0001; Mean ± SEM, Unpaired t-tests, n = 4 independent lines/group.

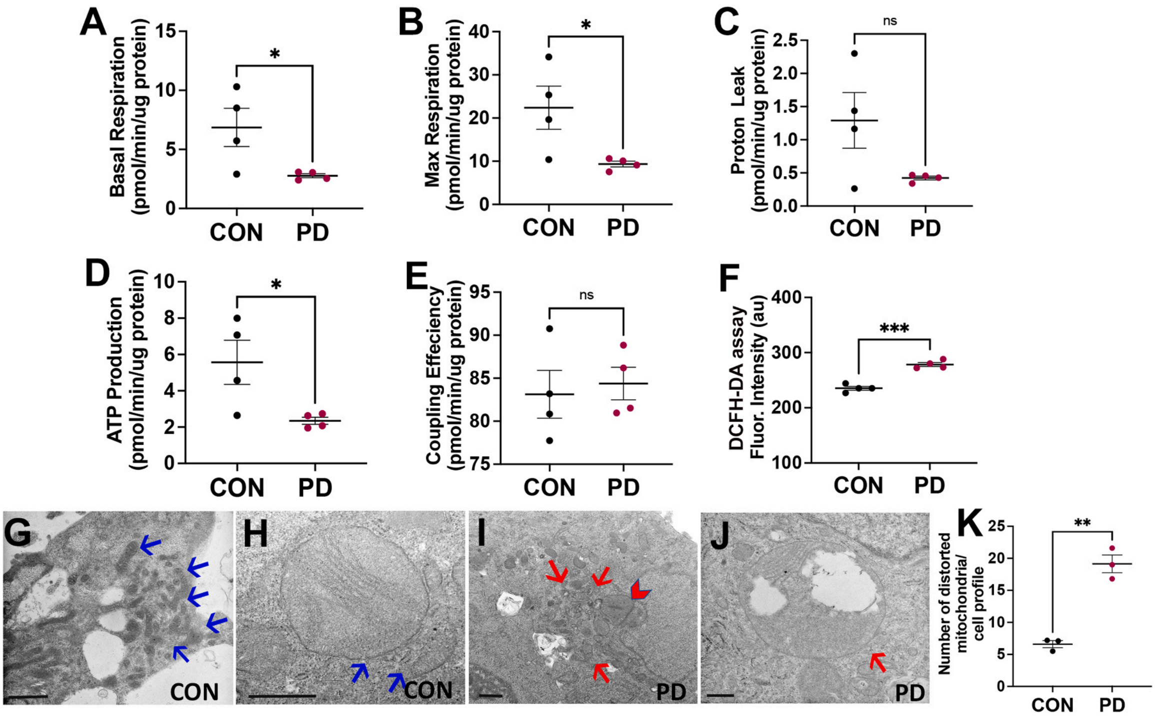

Fig. 6. : Mitochondrial dysfunction in the PD iPSC-DAN. (A-E) shows results from a Seahorse Mito Stress test, specifically basal respiration (A), maximal respiration (B), proton leak (C), ATP production (D) and coupling efficiency (E), performed on Day 50 DA CON and PD iPSC-DAN. Total cellular ROS level comparisons (DCFH-DA assay) between the CON and PD iPSC-DAN is in (F). TEM images showing the observed ultrastructure of mitochondria in CON and PD iPSC-DAN (G, H, red arrows point to normal mitochondria; I, J, red arrows point to distorted mitochondria, red arrowhead – swollen mitochondrion, vacuolating mitochondrion is seen in J). Quantification of the number of distorted mitochondria in PD vs CON iPSC-DAN is in (K). Scale Bars: (G-J): 500 nm. *p < 0.05, p < 0.001; Mean ± SEM, Unpaired t-tests, n = 4 independent lines/group.

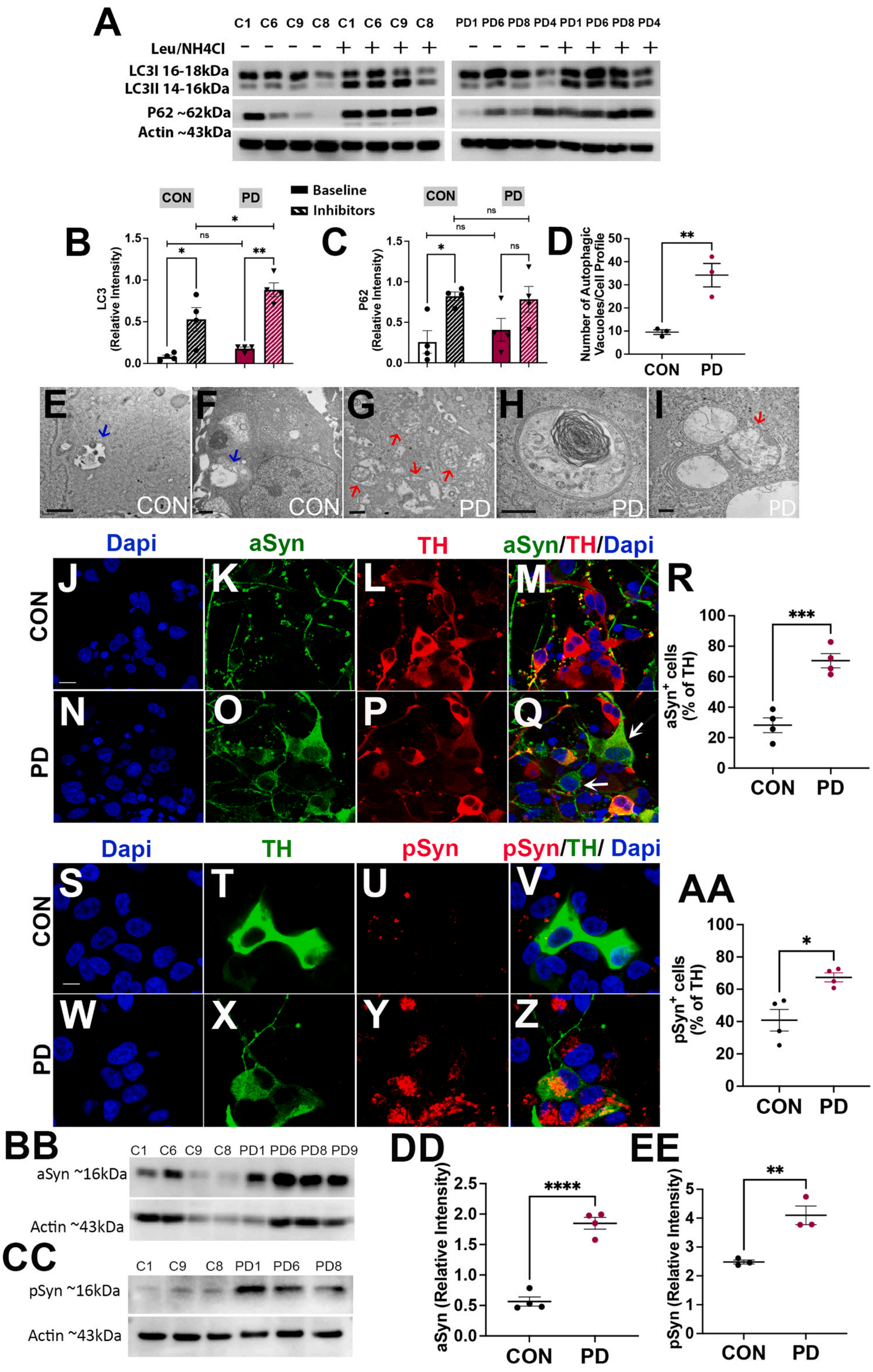

Fig. 7. : Autophagy assessments in the fibroblast matched iPSC-DAN. (A) shows western blot data from CON and PD iPSC-DAN showing LC3 and P62 turnover at baseline and after treatment with a combination of NH4Cl/ Leup. Densitometric quantification is in (B, C). Overall, two-way RM ANOVA analyses showed no significant interaction between group (C and PD) and treatment (+/- inhibitors), but indicated that the effect of treatment was highly significant in relation to LC3 ($P < 0.0005$, $F_{1,}$ $6 =$ 46.57) and P62 ($P < 0.0028$, $F_{1,6} = 23.59$). The effect of the group was also significant in relation to LC3 ($P < 0.0336$, $F_{1,\ 6} = 7.65$). Representative TEM images of CON and PD iPSC-DAN, showing the relative presence of autophagic vesicles is in (E-I), with the associated quantification in (D). Red arrows point to autophagic vesicles in CON cells and blue arrows indicate those in PD cells. (H) shows a typical double membraned autophagosome in a PD iPSC-DAN, whereas (I) shows autolysosomes with different constituents, including engulfed mitochondria (red arrow in I). (J-Q) and (S-Z) show comparative images of CON vs PD iPSC-DAN immunostained with antibodies against aSyn/TH and pSyn/TH, with associated quantification in (R, AA). Expression of aSyn and pSyn was also assessed via western blotting (BB-EE). Scale Bars: (E-I) = 500 nm, (J-Q) = 20 μm, (S-Z) = 30 μm. $*p < 0.05$, $* *p < 0.01$, $* ** *p < 0.0001$; Mean ± SEM, two-way ANOVAs in (B, C), Unpaired t-tests in (D), n = 4 independent lines/group.

cells (Fig. 1**H**; p = 0.0108, Unpaired t-test, t = 2.910, df=15).

The morphology of the fibroblasts was also assessed. Specifically, the fibroblasts were stained with Phalloidin and DAPI to allow clear demarcations of cell size and shape, and subsequently analyzed via the CellProfiler software (Fig. 1**I**). Cell size (area and perimeter), form factor, and eccentricity were estimated. On average, PD cells had significantly lower area (Fig. 1**K**; p = 0.0324, Unpaired t-test, t = 2.357, df=15) and perimeter (Fig. 1**L**; p = 0.0154, Unpaired t-test, t = 2.734, df=15), indicating that they were smaller compared to control cells. Eccentricity (a measure of cell elongation) and form factor (a measure of roundness) are indicators of cell shape. It was seen that although PD and control cells were both elongated (Fig. 1**N**), PD fibroblasts were significantly more defined (less ramified and rounder) than control fibroblasts (Fig. 1**M**; p = 0084, Unpaired t-test, t = 3.034, df=15). These data demonstrate that PD fibroblasts distinctly differed in terms of both their growth and morphological characteristics from controls.

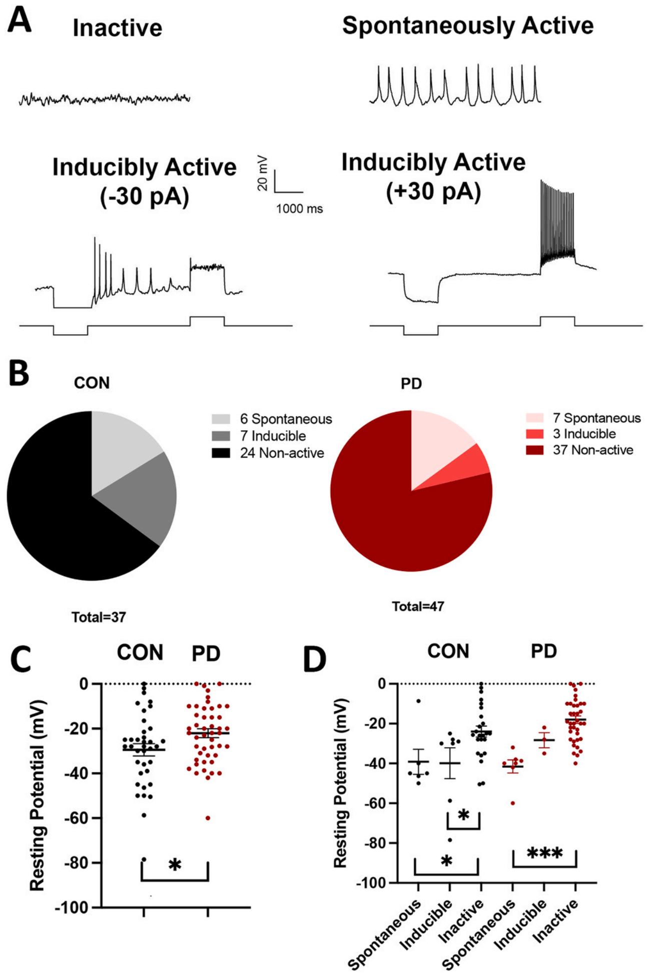

Fig. 8. : Electrophysiological analysis of CON and PD iPSC-DAN. Day 55 iPSC-DAN were subjected to whole cell recordings and analyzed for spontaneous and evoked action potentials. Representative current-clamp recordings of inactive, spontaneously active, and inducible active neurons (with −30 pA current step, and +30 pA step) are in (A). Summary of type of cell activity between CON and PD neurons ($p = 0.197$, Fisher's exact test) is shown in (B). (C) depicts a comparison of the mean resting potential between CON and PD neurons. Dots represent data values for individual cells. (D) displays the differences in mean resting potential by activity of spontaneous, inducible, and inactive neurons between CON and PD groups. $*p < 0.05$, $* *p < 0.01$, $* **p < 0.001$; Mean ± SEM, one-way ANOVA with Student-Newman-Keuls posthoc test in (C), two-way ANOVA with Student-Newman-Keuls posthoc test in (D), $n = 3$ independent lines/group.

3.2. PD fibroblasts exhibit impaired mitochondrial structure and function

We assessed mitochondrial function in the fibroblasts using the Seahorse Mito Stress test (Fig. 2). The primary function of mitochondria is oxidative phosphorylation (OXPHOS) to produce the majority of ATP. Apart from their metabolic function, the mitochondria also play a crucial role in reactive oxygen species (ROS) generation (Murphy, 2009; Venditti et al., 2013). The Seahorse Mito Stress test estimates key parameters of mitochondrial function by directly measuring the oxygen consumption rate (OCR) of cells after the addition of specific modulators of respiration (Gu et al., 2021; Teves et al., 2017). Fig. 2**A** illustrates the complexes of the Electron Transport Chain (ETC) and target of action of the modulators used in the Seahorse Mito Stress test which then reveals the key parameters of mitochondrial function, some of which are depicted in Fig. 2**C.** Firstly, it was found that PD cells had significantly higher basal (Fig. 2**B**; $p = 0.0143$; Unpaired t-test; $t = 2.794$, df=14) and maximal respiration rates (Fig. 2**D**; $p = 0.0470$; Unpaired t-test, $t = 2.178$, df=14). In concert with these findings, proton leak (PL) was noted to be significantly higher (Fig. 2**E**; $p = 0.0078$; Unpaired t-test, $t = 3.100$, df=14), whereas coupling efficiency (CE) was significantly lower (Fig. 2**F**; $p = 0.0193$; Unpaired t-test, $t = 2.643$, df=14), suggesting that the increased PL may be the cause of increased oxygen consumption rates and lower ATP reserve in PD cells. However, there were no significant differences in ATP levels between PD and control cells (Fig. 2**G**). Non-mitochondrial respiration and spare respiratory capacity also showed no significant differences between PD and control fibroblasts (**Supp.** Fig. 1**A, B**). Total reactive oxygen species (ROS) levels, measured by DCFH-DA fluorescence which represents peroxide species, was also elevated in the PD cells compared to controls (Fig. 2**H**; $p = 0.0085$; Unpaired t-test, $t = 3.027$, df=15). In essence, these data indicated altered OXPHOS in the PD fibroblasts. Moreover, in terms of glycolysis, extracellular acidification rate (ECAR) measurements indicated that basal ($p = 0.0128$, Unpaired t-test, $t = 2.854$, df=14) and maximal ECAR ($p = 0.0302$, Unpaired t-test, $t = 2.412$, df=14) were significantly higher in the PD fibroblasts, however the OCR/ECAR ratio was not altered suggesting no greater reliance of the PD cells on glycolysis versus OXPHOS (**Supp.** Fig. 1**C-F**).

Given the mitochondrial alterations noted in PD fibroblasts, we proceeded to examine the morphology of the mitochondria in more detail via transmission electron microscopy (TEM). Here, it was observed that while control cells showed normal mitochondrial ultrastructure, with expected shape, size, and intact cristae structures (Fig. 2**I, J**, blue arrows), many mitochondria in PD fibroblasts were smaller, misshaped, and lacked typical cristae (Fig. 2**K, L**, red arrows). Quantification showed that there were higher numbers of such distorted mitochondria in PD cells compared to controls (Fig. 2**M**; $p < 0.0001$; Unpaired t-test, $t = 6.275$, df=13). Supporting these data, when mitochondrial networks were visualized using ATPIF1 targeted antibodies, PD fibroblasts showed a distinctly altered mitochondrial morphology than controls (Fig. 2**N**). Systematic fractal analysis of the mitochondrial structure of individual cells via NIH Image J (Fig. 2**O)** indicated that PD cells on average had significantly reduced pixel density (Fig. 2**P;** $p = 0.0068$; Unpaired t-test, $t = 3.324$, df=156), significantly higher lacunarity (Fig. 2**Q;** $p = 0.0551$; Unpaired t-test, $t = 2.745$, df=156), and lower fractal dimension (Fig. 2**R;** $p = 0.0551$; Unpaired t-test, $t = 1.932$, df=156), indicating reduced complexity and more 'gappiness' of mitochondrial networks. These data together suggested less contiguous and a more fragmented mitochondrial structure in the PD cells. Additionally, skeleton analysis showed that the number of endpoints/skeleton (Fig. 2**S;** $p = 0.0062$; Unpaired t-test, $t = 2.778$, df=138) was significantly reduced, while the number of endpoints/area was increased (Fig. 2**T;** $p = 0.0521$; Unpaired t-test, $t = 1.956$, df=165), in PD mitochondria, again suggesting diminished complexity and greater fragmentation. Taken together, the mitochondrial structural and functional data implied a baseline mitochondrial dysfunction in the PD fibroblasts.

3.3. PD fibroblasts display autophagic dysregulation

Impaired autophagy is known to be an important process contributing to PD pathology, as evidenced by the collection of toxic, aggregate-prone, intracytosolic proteins in afflicted cells (Cuervo et al., 2010; Menzies et al., 2015). Our previous studies, as well as others, have shown autophagic changes in fibroblasts from both genetic and sporadic PD subjects (Galvagnion et al., 2022; Gonzalez-Casacuberta et al., 2019; Teves et al., 2017). From this perspective, we examined autophagy in the fibroblast lines, particularly in relation to the macroautophagy pathway (Fig. 3**A**). Using immunoblotting, we examined the expression of the two standard autophagy markers, LC3 and p62. These experiments showed that, at baseline, LC3II levels were significantly lower in the PD fibroblast lines as compared to controls (Fig. 3**B, D;** $p = 0.0127$, two-way RM ANOVA with Tukey's multiple comparison test). To understand whether the lower LC3II was due to the reduced production or

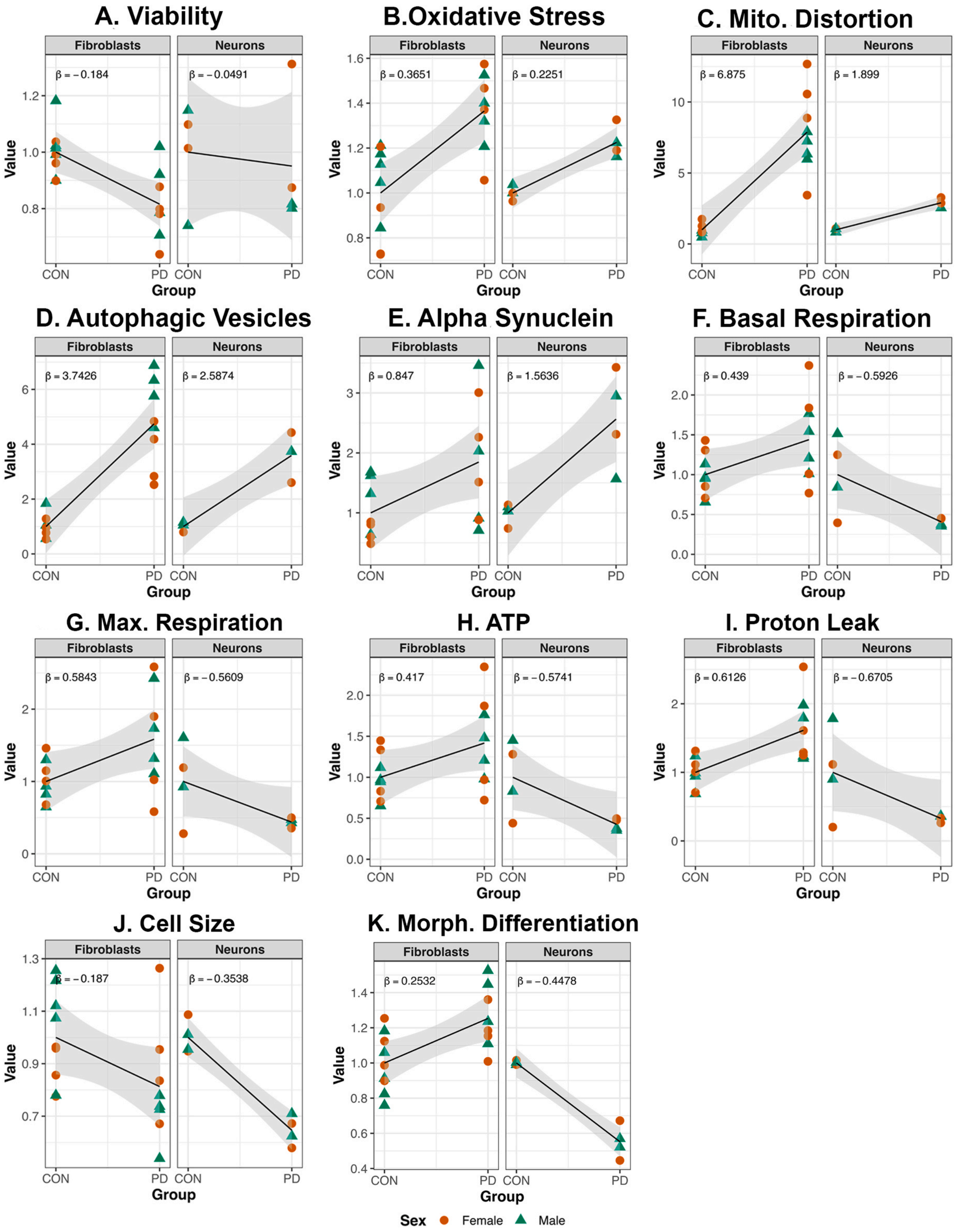

Fig. 9. : The scatterplots display a side-by-side comparison between fibroblast and neurons on the relationship between CON and PD groups and sex for different cellular assays. Specifically, the results shown compare fibroblast to neuron viability (A, MTT assay), oxidative stress (B, DCFH-DA assay), number of distorted mitochondria (C, electron microscopy), number of autophagic vesicles (D, electron microscopy), alpha-synuclein (E), basal respiration (F, seahorse assay), maximal respiration (G, seahorse assay), ATP production (H, seahorse assay), and proton leak (I, seahorse assay), cell size (J, Image J) and morphological differentiation (K, Image J, comparison of form factor in fibroblasts to the number of neurites in neurons, both these parameters measure process ramification). The data has been modified to represent fold changes compared to the mean of controls. The line in each plot represents the change between the mean values of the groups (CON vs PD), and the slope of the line (β) is the difference between PD and CON means. The shaded area represents 95% confidence interval for the placement of the line.

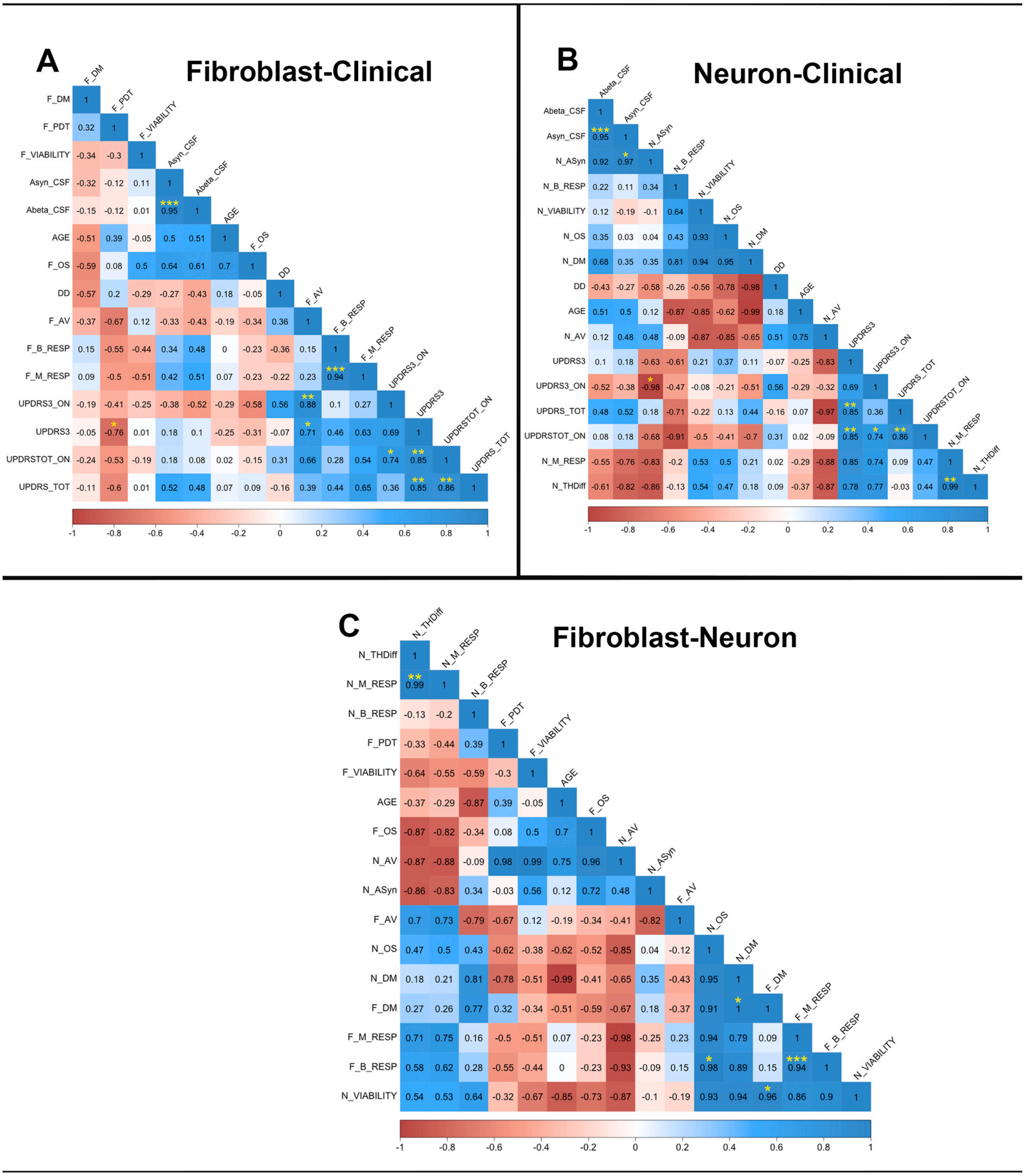

A Fibroblast-Clinical

	F_DM	F_PDT	F_VIABILITY	Asyn_CSF	Abeta_CSF	AGE	F_OS	DD	F_AV	F_B_RESP	F_M_RESP	UPDRS3_ON	UPDRS3	UPDRSTOT_ON	UPDRS_TOT
F_DM	1														
F_PDT	0.32	1													
F_VIABILITY	-0.34	-0.3	1												
Asyn_CSF	-0.32	-0.12	0.11	1											
Abeta_CSF	-0.15	-0.12	0.01	*** 0.95	1										
AGE	-0.51	0.39	-0.05	0.5	0.51	1									
F_OS	-0.59	0.08	0.5	0.64	0.61	0.7	1								
DD	-0.57	0.2	-0.29	-0.27	-0.43	0.18	-0.05	1							
F_AV	-0.37	-0.67	0.12	-0.33	-0.43	-0.19	-0.34	0.36	1						
F_B_RESP	0.15	-0.55	-0.44	0.34	0.48	0	-0.23	-0.36	0.15	1					
F_M_RESP	0.09	-0.5	-0.51	0.42	0.51	0.07	-0.23	-0.22	0.23	*** 0.94	1				
UPDRS3_ON	-0.19	-0.41	-0.25	-0.38	-0.52	-0.29	-0.58	0.56	** 0.88	0.1	0.27	1			
UPDRS3	-0.05	* -0.76	0.01	0.18	0.1	-0.25	-0.31	-0.07	* 0.71	0.46	0.63	0.69	1		
UPDRSTOT_ON	-0.24	-0.53	-0.19	0.18	0.08	0.02	-0.15	0.31	0.66	0.28	0.54	* 0.74	** 0.85	1	
UPDRS_TOT	-0.11	-0.6	0.01	0.52	0.48	0.07	0.09	-0.16	0.39	0.44	0.65	0.36	** 0.85	** 0.86	1

B Neuron-Clinical

	Abeta_CSF	Asyn_CSF	N_ASyn	N_B_RESP	N_VIABILITY	N_OS	N_DM	DD	AGE	N_AV	UPDRS3	UPDRS3_ON	UPDRS_TOT	UPDRSTOT_ON	N_M_RESP	N_THDiff
Abeta_CSF	1															
Asyn_CSF	*** 0.95	1														
N_ASyn	0.92	* 0.97	1													
N_B_RESP	0.22	0.11	0.34	1												
N_VIABILITY	0.12	-0.19	-0.1	0.64	1											
N_OS	0.35	0.03	0.04	0.43	0.93	1										
N_DM	0.68	0.35	0.35	0.81	0.94	0.95	1									
DD	-0.43	-0.27	-0.58	-0.26	-0.56	-0.78	-0.98	1								
AGE	0.51	0.5	0.12	-0.87	-0.85	-0.62	-0.99	0.18	1							
N_AV	0.12	0.48	0.48	-0.09	-0.87	-0.85	-0.65	0.51	0.75	1						
UPDRS3	0.1	0.18	-0.63	-0.61	0.21	0.37	0.11	-0.07	-0.25	-0.83	1					
UPDRS3_ON	-0.52	-0.38	* -0.98	-0.47	-0.08	-0.21	-0.51	0.56	-0.29	-0.32	0.69	1				
UPDRS_TOT	0.48	0.52	0.18	-0.71	-0.22	0.13	0.44	-0.16	0.07	-0.97	** 0.85	0.36	1			
UPDRSTOT_ON	0.08	0.18	-0.68	-0.91	-0.5	-0.41	-0.7	0.31	0.02	-0.09	** 0.85	* 0.74	** 0.86	1		
N_M_RESP	-0.55	-0.76	-0.83	-0.2	0.53	0.5	0.21	0.02	-0.29	-0.88	0.85	0.74	0.09	0.47	1	
N_THDiff	-0.61	-0.82	-0.86	-0.13	0.54	0.47	0.18	0.09	-0.37	-0.87	0.78	0.77	-0.03	0.44	** 0.99	1

C Fibroblast-Neuron

	N_THDiff	N_M_RESP	N_B_RESP	F_PDT	F_VIABILITY	AGE	F_OS	N_AV	N_ASyn	F_AV	N_OS	N_DM	F_DM	F_M_RESP	F_B_RESP	N_VIABILITY
N_THDiff	1															
N_M_RESP	** 0.99	1														
N_B_RESP	-0.13	-0.2	1													
F_PDT	-0.33	-0.44	0.39	1												
F_VIABILITY	-0.64	-0.55	-0.59	-0.3	1											
AGE	-0.37	-0.29	-0.87	0.39	-0.05	1										
F_OS	-0.87	-0.82	-0.34	0.08	0.5	0.7	1									
N_AV	-0.87	-0.88	-0.09	0.98	0.99	0.75	0.96	1								
N_ASyn	-0.86	-0.83	0.34	-0.03	0.56	0.12	0.72	0.48	1							
F_AV	0.7	0.73	-0.79	-0.67	0.12	-0.19	-0.34	-0.41	-0.82	1						
N_OS	0.47	0.5	0.43	-0.62	-0.38	-0.62	-0.52	-0.85	0.04	-0.12	1					
N_DM	0.18	0.21	0.81	-0.78	-0.51	-0.99	-0.41	-0.65	0.35	-0.43	0.95	1				
F_DM	0.27	0.26	0.77	0.32	-0.34	-0.51	-0.59	-0.67	0.18	-0.37	0.91	* 1	1			
F_M_RESP	0.71	0.75	0.16	-0.5	-0.51	0.07	-0.23	-0.98	-0.25	0.23	0.94	0.79	0.09	1		
F_B_RESP	0.58	0.62	0.28	-0.55	-0.44	0	-0.23	-0.93	-0.09	0.15	* 0.98	0.89	0.15	*** 0.94	1	
N_VIABILITY	0.54	0.53	0.64	-0.32	-0.67	-0.85	-0.73	-0.87	-0.1	-0.19	0.93	0.94	* 0.96	0.86	0.9	1

Fig. 10. **:** Correlation matrices comparing clinical data obtained at the time of sample collection to results from the fibroblast assays (A, Fibroblast-Clinical), and the neuronal assays (B, Neuron-Clinical) are shown. (C, Fibroblast-Neuron) displays the correlation matrix between cellular data from neurons and cellular data from the fibroblasts. Age (age at sample collection) and DD (disease duration) are included in all the correlation matrices. Pearson correlation coefficients are shown. Negative correlation coefficients are depicted in red, while positive correlation coefficients are depicted in blue. The magnitude of the coefficient is indicated by the color intensity. The diagonal shows the correlation of each variable with itself which is a perfect 1. Significant correlations using a two-tailed test are indicated with asterisks: * $p < 0.05$, * ** $p < 0.01$, * ** $p < 0.001$.

increased degradation of LC3II, the cells were treated with a combination of ammonium chloride and leupeptin (NH4Cl/Leup, lysosomal inhibitors) to measure autophagic flux (Fig. 3**A**). Upon this treatment, a significantly increased accumulation of LC3II was noted in PD cells (Fig. 3**B, D;** $p < 0.0001$, two-way RM ANOVA, Tukey's multiple comparison test) indicating higher LC3II degradation/turnover. In fact, in the PD lines, on average LC3II levels increased ~ 10 fold from baseline after inhibitor treatment (Fig. 3**D**; change in relative intensity from

0.082 to 0.881), compared to a ∼ 4 fold increase in control lines (Fig. 3**D**; 0.183–0.840). Furthermore, under starvation conditions, although greater LC3II expression was observed in both PD and control lines at baseline, the increase was statistically significant in the PD group (Fig. 3**C, D**; $p = 0.0460$, two-way RM ANOVA, Tukey's multiple comparison test) suggesting greater autophagy. Treatment with NH_4Cl/Leup further exaggerated the increase in LC3II in both control ($p = 0.0005$) and PD ($p = 0.0003$) lines (Fig. 3**C, D**; two-way RM ANOVA, Tukey's multiple comparison test). In terms of p62, no significant differences in p62 expression were seen at baseline, in PD vs controls (Fig. 3**B, E**). However, P62 expression significantly increased upon exposure to a NH_4Cl/Leup in control ($p = 0.0494$) but not PD lines (Fig. 3**B, E;** two-way RM ANOVA, Tukey's multiple comparison test). On the other hand, compared to serum conditions, P62 levels were reduced at baseline upon starvation in both control ($p = 0.0297$) and PD ($p = 0.0029$) lines (Fig. 3**C, E;** two-way RM ANOVA, Tukey's multiple comparison test). However, although treatment with NH_4Cl/Leup resulted in significant P62 increases in both control ($p = 0.0002$) and PD ($p = 0.0014$) lines, compared to baseline (two-way RM ANOVA, Tukey's multiple comparison test), a significantly greater elevation was seen in control cells vs PD (Fig. 3**C, E;** $p = 0.0358$, two-way RM ANOVA, Tukey's multiple comparison test). All in all, these data suggested the presence of higher autophagic load and processing in the PD fibroblasts.

To further probe the autophagic changes, we examined the fibroblasts in more detail via TEM. It was seen that while control cells showed the presence of some autophagic vesicles (AVs, Fig. 3**F, G**; blue arrows), sporadic PD fibroblasts exhibited a significantly increased collection of autophagic structures with varied cargo (Fig. 3**H, I**, red arrows). Quantification revealed a significant accumulation of AVs in the sporadic PD cells than in the control cells (Fig. 3**J**; $p < 0.0001$, Unpaired t-test, $t = 6.105$, df=13). These results suggested an alteration of autophagic activity in the PD fibroblasts compared to control cells.

3.4. Characterization of the growth, differentiation, and morphology of midbrain DA neurons generated from matched iPSCs derived from the same patient fibroblast lines

We next differentiated a group of matched iPSC lines (four control and four PD) generated from a subset of the fibroblast lines used in the first part of this study. Specifically we derived midbrain DA neurons, using a modified floor plate-based approach involving dual SMAD inhibition by adapting a previous method (Fig. 4**a-d; schema in Methods section**) (Chambers et al., 2009; Kriks et al., 2011). A more detailed description of the differentiation method has been included in the supplementary methods section. The cells were characterized for various neuronal and dopaminergic differentiation markers at 25- and 50-days post-differentiation. As shown, at day 25, robust differentiation into $Tuj1^+$ neurons was observed (Fig. 4**A, C**). Quantification revealed that on average, the percentage of $Tuj1^+$ cells was significantly lower in the PD cultures compared to controls (Fig. 4**E**; $p = 0.0203$; Unpaired t-test, $t = 3.132$, df=6). No significant differences in the percentage of cells expressing the DA neuron marker, Tyrosine Hydroxylase (TH), were found at this stage (Fig. 4**B, D, F**). We also assessed other markers indicative of midbrain DA neuron specification, mainly Lmx1a and Foxa2. As seen, although strong Lmx1a expression was seen (Fig. 4**G-N**), there were significantly lower numbers of $Lmx1a^+$ neurons in the PD cultures vs controls (Fig. 4**O**; $p = 0.0285$, Unpaired t-test, $t = 2.869$, df=6). No statistically significant differences were found between the percentage of Foxa2 expressing cells between PD and control, and most TH cells were $Foxa2^+$ (Fig. 4**P-W, X**).

At day 50 post-differentiation, we examined the cells for the expression of TH and Girk2. As known, TH/$Girk2^+$ co-expression specifically marks mature A9 subtype DA neurons of the lateral tier of the substantia nigra (SN) that particularly degenerate in PD (Barker et al., 2015). It was found that while there was efficient differentiation into A9 DA neurons (Fig. 4**Y, Z, AA-FF**), there were lower percentages of TH^+ and TH/Girk2 double-positive cells in PD vs control cultures (Fig. 4 **GG, HH**; $p = 0.0084$, Unpaired t-tests, $t = 3.858$, df=6). Compared to ∼67% and 96% in control cultures, only ∼60% and 89% of cells were TH^+ and TH/$Girk2^+$, respectively in the PD cultures. When the cellular viability was assessed at day 50 post-differentiation, no statistically significant differences on average were seen between PD and control lines **(**Fig. 5**C;** Fig. 5**A, B** shows representative phase images of PD and control cultures**)**. Nevertheless, it was interesting to note that all PD lines, besides one, exhibited reduced viability than controls. We also examined the morphology of the cells by comparing MAP2 stained neurons in control and PD cultures (Fig. 5**D-E, G-H**). It was observed that in contrast to controls, PD neurons appeared smaller and had lesser neurite extensions. When the soma size and the number of neurites was measured (NIH ImageJ software), it was confirmed that the PD neurons indeed had significantly smaller soma sizes (Fig. 5**F**, $p = 0.0002$, Unpaired t-test, $t = 8.226$, df=6) as well as a significantly lesser number primary neurites projecting from the cell body (Fig. 5**I**, $p < 0.0001$, Unpaired t-test, $t = 9.373$, df=6).

3.5. Mitochondrial structure and function are highly compromised in the PD DA neurons

Similar to the fibroblasts, the mitochondrial function of the midbrain DA neurons was examined using the Seahorse Mito Stress test. It was found that the basal (Fig. 6**A**; $p = 0.0457$, Unpaired t-test, $t = 2.513$, df=6) and maximal respiration (Fig. 6**B**; $p = 0.0413$, Unpaired t-test, $t = 2.588$, df=6) of the PD DA neurons was significantly reduced, whereas no differences in PL were seen in the PD DA neurons compared to controls **(**Fig. 6**C)**. Additionally, there was a significant drop in ATP production in the PD DA neurons (Fig. 6**D**; $p = 0.0396$, Unpaired t-test, $t = 2.620$, df=6), with no significant differences seen in CE values (Fig. 6**E**). Non-mitochondrial was also compromised in the PD cells vs controls (**Supp.** Fig. 2**A**; $p = 0.0244$, Unpaired t-test, $t = 2.987$, df=6), and no alterations in spare respiratory capacity were seen (**Supp.** Fig. 2**B)**. Associated with these changes in mitochondrial respiration rates, a significant elevation of total ROS levels was also found in the PD DA neurons (Fig. 6**F**; $p = 0.0001$, Unpaired t-test, $t = 8.464$, df=6). Finally, basal ECAR rates were significantly lower in the PD DA neurons (**Supp.** Fig. 2**C**; $p = 0.0314$, Unpaired t-test, $t = 2.795$, df=6), however, the basal OCR to ECAR ratio was not significantly altered (**Supp.** Fig. 2**D**). The maximal ECAR was not significantly lower in the PD cells with no discernable changes in the maximal OCR to ECAR ratio (**Supp.** Fig. 2**E, F**). Overall, these data suggested a trend towards higher reliance on OXPHOS (than glycolysis) in the PD DA neurons. Furthermore, TEM analyses showed that while control cells had normal mitochondrial ultrastructure (Fig. 6**G, H**, blue arrows), mitochondria in the PD neurons showed altered shape, size and disruption of the typical cristae arrangement (Fig. 6**I**, red arrows, red arrowhead – swollen mitochondrion, **J** shows a vacuolating mitochondrion). Upon quantification, it was determined that there were significantly more such distorted mitochondria in PD cells compared to controls (Fig. 6**K**; $p = 0.0011$; Unpaired t-test, $t = 8.397$, df=4).

3.6. Autophagic function and alpha synuclein expression is altered in the PD DA neurons

Autophagy, an essential catabolic mechanism for degradation of misfolded proteins and damaged organelles, is known to be affected in PD brain regions (Malkus et al., 2009). Thus, we investigated autophagy and the expression of alpha synuclein (aSyn), a known target of autophagy, in the DA neurons. It was seen that LC3II expression did not differ significantly at baseline between control and PD neurons (Fig. 7**A**). However, treatment with the lysosomal inhibitor combination of NH_4Cl/Leup resulted in a more significant increase in LC3II in PD cells than controls, indicating a potentially higher LC3II degradation/turnover (Fig. 7**A, B,** treated CON vs treated PD, $p = 0.0220$, two-way RM

ANOVA with Sidak's multiple comparisons test). On average, after inhibitor treatment, LC3II levels increased ~7 fold from baseline (relative intensity increased from 0.147 to 0.998) in the PD lines, compared to a ~ 5 fold increase in the control cells (0.099–0.502). In terms of p62 expression, PD and controls did not show statistically significant differences at baseline (Fig. 7**A, C**). However, upon exposure to NH4Cl/Leup, p62 expression increased significantly in the control cells Fig. 7**C,** $p = 0.0124$, two-way RM ANOVA with Sidak's multiple comparisons test), whereas PD cells did not show a statistically significant elevation (Fig. 7**C**). Altogether, these data suggested the presence of higher basal autophagy and greater autophagic load in PD DA neurons.

Moreover, supporting the western blotting data, TEM analysis showed that although control cells contained some autophagic vesicles (Fig. 7**E, F**; blue arrows), sporadic PD neurons exhibited a striking accumulation of autophagic structures in their cytoplasm (Fig. 7**G**, red arrows). As shown, typical double membraned autophagosomes (Fig. 7**H**) and autolysosomes with different cargoes (Fig. 7**I,** red arrow points to engulfed mitochondria) were observed. When the number of autophagic vesicles were enumerated, as expected, significantly higher numbers were seen in PD neurons (Fig. 7**D**, $p = 0.0088$, Unpaired t-test, $t = 4.770$, df=4). Essentially, these data in totality suggested dysregulated autophagy in PD DA neurons.

Assessment of the PD-relevant protein, aSyn, via immunocytochemical analysis showed that TH$^+$ DA neurons in PD cultures had higher aSyn expression within their cell bodies compared to controls (Fig. 7**J-Q).** Interestingly, many PD neurons with high intracytoplasmic aSyn showed reduced TH immunoreactivity suggesting dopaminergic dysfunction (white arrows in **7Q**). These qualitative impressions were confirmed through quantitative analysis, which revealed significantly more aSyn expressing TH$^+$ neurons in PD than control cultures (Fig. 7**R**; $p = 0.0008$, Unpaired t-test, $t = 6.270$, df=6). Furthermore, PD cultures generally had more aSyn expression compared to controls (**Supp.** Fig. 3**A-F**). In fact, both the number of aSyn expressing cells and the relative intensity of aSyn expression was higher in the PD cultures than in controls indicating higher aSyn load in the PD group (**Supp.** Fig. 3**G;** $p = 0.0012$, Unpaired t-test, $t = 5.746$, df=6; **Supp**. Fig. 3**H;** $p = 0.0092$, Unpaired t-test, $t = 3.783$, df=6). Furthermore, increased aSyn expression in the PD DA neurons was supported by data from western blotting studies, which showed a similar trend (**Fig. 7BB, DD;** $p < 0.001$, Unpaired t-test, $t = 10.56$, df=6; full blots shown in Supp. Fig. 4A,B**).** Moreover, expression of the pathological aSyn epitope, pSer129 was also found to be higher in TH$^+$ DA neurons in PD lines compared to controls via immunostaining (Fig. 7**S-Z**; $p = 0.0105$, Unpaired t-test, $t = 3.665$, df=6) and immunoblotting (**Fig. 7CC; EE,** $p = 0.0080$, Unpaired t-test, $t = 4.915$, df=4; full blots shown in Supp. Fig. 4C, D). Due to the autophagic dysregulation seen in PD neurons, the buildup of aSyn and pSyn in these cells may be attributed to inefficient autophagic clearance [34]. Given these results, as a comparison, we also assessed aSyn expression in the fibroblasts. Immunocytochemistry revealed higher aSyn in the PD fibroblasts than controls, although the levels were seen to be generally low across the groups (**Supp.** Fig. 3**I-K;** $p = 0.0143$, Unpaired t-test, $t = 2.77$, df=15). Nonetheless, western blotting and dot blot analysis did not detect aSyn in any of the lines.

3.7. PD DA neurons express different electrophysiological properties from controls

The electrophysiological activity of PD and control neurons was analyzed at rest and after current injections to attempt to induce spiking. The different types of spiking activity profiles seen are depicted in Fig. 8**A**. There was no statistically significant difference in type of activity between the PD and CON neurons (Fig. 8**B**, $p = 0.19$, Fisher's exact test). However, a greater proportion of PD neurons were non-active. Overall, it was found that 77% of PD neurons were non-active, showing no spiking either spontaneously at rest or when induced with current steps. In contrast, only 65% of control neurons were non-active, suggesting that the PD neurons were less active as a population (Fig. 8**B**). Although similar proportions of control and PD neurons had spontaneous spiking (16% vs. 15%), PD neurons had a much smaller proportion of cells with inducible spiking (19% vs. 6%). All inducible neurons but one showed spiking after a − 30pA current step while one showed spiking after a + 30pA step (Fig. 8**A**, bottom). This suggests the Na$^+$ channels were in an inactive state at baseline. Furthermore, both groups had fairly depolarized resting membrane potentials for mature neurons. However, control neurons had significantly more negative resting membrane potentials than PD neurons (Fig. 8**C**; control: -29 ± 2.73; PD: -22 ± 1.98 mV; $p < 0.05$, one-way ANOVA with SNK posthoc test, $F_{1,\,83} = 5.032$). There were no differences in resting membrane potential between the four cell lines of either control or PD. In addition, mean resting membrane potentials of spontaneously active cells were significantly lower than those of inactive cells (spontaneous: -40 ± 3.25; non-active: -20 ± 1.59 mV, $p < 0.001$; two-way ANOVA with SNK posthoc test, $F_{1,\,72} = 13.884$). When broken down by activity and group, spontaneously active neurons had lower resting membrane potentials than inactive neurons in control (Fig. 8**D**; spontaneous: -39 ± 5.3; non-active: -24 ± 2.65 mV, $p = 0.012$) and PD cultures (spontaneous: -42 ± 4.9; non-active: -18 ± 2.1 mV, $p < 0.001$; two-way ANOVA with SNK posthoc test, $F_{1,\,43} = 14.102$).

Since our data indicated a reduced soma size in PD neurons, we also assessed cellular capacitance. However, an analysis of cell capacitance showed no significant difference between control and PD neurons (Table 2: $p = 0.617$). There was also no significant difference in cell capacitance between cell lines within groups. Since neurons that were successfully recorded from had less variability in size as compared to the population of plated cells, cell capacitance measures may not be a good representation of the neuron sizes as a whole population.

Action potentials of spontaneously firing neurons were also analyzed. It should be noted that there was a large amount of variability in spiking between spontaneously active neurons. Some neurons spiked as many as 324 times during a 2-minute recording and one neuron only spiked twice. There were no differences in peak amplitude, decay tau, inter-event interval, or time to peak of spontaneous spikes between

Table 2
Electrophysiological Data.

Group	Parameter	Mean	95% CI	N Value	P Value
Control	Capacitance	12.05 (pF) Median	-1.47–2.61	36	0.579
PD		11.84 (pF) Median		46	
Control	Capacitance (Spontaneous)	9.34 (pF)	-10.02–2.26	6	0.186
PD		12.99 (pF)		7	
Control	Frequency (Spontaneous)	0.7 (hz)	-221.86 – 139.19	3	0.605
PD		1.13 (hz)		6	
Control	Peak Amplitude (Spontaneous)	38.52 (mV)	-13.11 – 13.78	3	0.955
PD		38.19 (mV)		6	
Control	Decay Tau (Spontaneous)	338.21 (ms)	-181.80 – 560.12	3	0.267
PD		149.047 (ms)		6	
Control	Inter-event Interval (Spontaneous)	1262.76 (ms) Median	-8249.58 – 5349.05	3	0.629
PD		930.08 (ms) Median		6	
Control	Time to Peak (Spontaneous)	174.51 (ms)	-10.46 – 191.41	3	0.072
PD		84.04 (ms)		6	

control and PD neurons (Table 2).

3.8. *Cross correlation analyses of fibroblast, DA neuron, and clinical data*

We compared the cellular data obtained from the fibroblasts and neurons to each other and correlated the cellular data from each of the cell types to some available clinical data from individual PD subjects. The scatterplots in Fig. 9, display the relationship between the groups (control and PD) and sex for different fibroblast and DA neuron assays, side by side, to allow for pairwise comparison. The data is expressed as fold changes normalized to mean of controls, and the line in each plot represents the change between the mean value of each group. The slope of the line represents difference between PD and CON means, and the shaded indicates the 95% confidence interval for the placement of the line, which is directly linked to the dispersion in the data point. As seen, the PD group on average showed reduced viability in the fibroblast but not in the neurons, however, the change was similar in both types of cells (Fig. 9**A;** Table 3). Regarding oxidative stress, PD showed a similar increase in values in both the fibroblasts and neurons (Fig. 9**B;** Table 3). Similarly, the changes in number of distorted mitochondria and number of AVs trended in the same direction for both fibroblasts and neurons (Fig. 9**C, D;** Table 3). While the amount of change was similar for both types of cells in the AV assay, for distorted mitochondrial number the change in fibroblasts was higher than in neurons (fibroblast: β_F=6.8750, SE_F=1.0956; neurons: β_N =1.8990, SE_N =0.2261; $t_{15.14}$ =4.4481; p-value=0.0005). Furthermore, the relative expression of alpha synuclein was higher in both PD neurons and PD fibroblasts compared to their control counterparts showing fibroblast and neurons a similar amount of change (Fig. 9**E and** Table 3).

Interestingly, with respect to the mitochondrial function measures, the directionality of changes was contrary between the fibroblasts and DA neurons: basal respiration (fibroblast: β_F=0.4390, SE_F=0.2130; neurons: β_N =−0.5926, SE_N =0.2456; t_{17} =3.1725; $p = 0.0056$), maximal respiration (fibroblast: β_F=0.5843, SE_F=0.2683; neurons: β_N =−0.5609, SE_N =0.2801; $t_{18.48}$ =2.9521; $p = 0.0084$), ATP production (fibroblast: β_F=0.4170, SE_F=0.2186; neurons: β_N =−0.5741, SE_N =0.2308; $t_{18.31}$ =3.1170; $p = 0.0059$), and PL (fibroblast: β_F=0.6126, SE_F=0.1854; neurons: β_N =−0.6705, SE_N =0.3267; $t_{11.67}$ =3.4161; $p = 0.0053$). For example, PD neurons had lower basal respiration, maximal respiration, ATP, and PL production, compared to control neurons (negative slopes), whereas fibroblasts showed the opposite trend (positive slopes). The amount of change in the positive or negative slopes were similar (Fig. 9**F-I;** Table 3). The cell size was reduced in both PD fibroblasts and the DA, and the change did not differ between cell types (Fig. 9**J;** Table 3**).** Lastly, morphological differentiation (Fig. 9**K)** increased in both PD fibroblasts (form factor; increases in form factor indicate reduced morphological differentiation) and the DA neurons (number of neurites), and this change was higher in the DA neurons (fibroblast: β_F=0.2532, SE_F=0.0834; neurons: β_N =0.8110, SE_N =0.0865; $t_{18.92}$ =4.6409; $p = 0.0002$; Table 3).

Three correlation matrices based on Pearson's correlation coefficient (r) were generated: (1) between specific clinical and cellular data for the fibroblasts (Fig. 10**A**, Fibroblast-Clinical), (2) between specific clinical and cellular data for neurons (Fig. 10**B**, Neurons-Clinical), and (3) between selected cellular assays of neurons and fibroblasts (Fig. 10**C,** Fibroblast-Neuron). All these plots show negative correlations coefficients in red and positive correlations coefficients in blue. Correlation values vary between the range of negative one and positive one, [− 1,1], and the matrix depicts correlations between all possible pairs of variables. The diagonal shows the correlation of each variable with itself, which is a perfect 1. Most pairwise correlations were not significant at the $\alpha = 0.05$. For the fibroblast-clinical correlation matrix (Fig. 10**A**), positive association were detected between Abeta_CSF and Asyn_CSF ($r = 0.95$, $p = 0.0003$, $N = 8$), F_M_RESP and F_B_RESP ($r = 0.94$, $p = 0.0004$, $N = 8$), UPDRS3_ON and F_AV ($r = 0.88$, $p = 0.0044$, $N = 8$), UPDRS3 and F_AV ($r = 0.71$, $p = 0.0484$, $N = 8$), UPDRSTOT_ON and UPDRS3_ON ($r = 0.74$, $p = 0.0345$, $N = 8$) and UPDRS3 ($r = 0.85$, $p = 0.0068$, $N = 8$), and UPDRS_TOT and UPDRS3 ($r = 0.85$, $p = 0.0069$, $N = 8$) and UPDRSTOT_ON ($r = 0.86$, $p = 0.0060$, $N = 8$). A negative association was detected between UPDRS3 and F_PDT ($r = -0.76$, $p = 0.0494$, $N = 7$). An interesting negative association between F_OS and UPDRS3_ON scores ($r = -0.36$, $p = 0.0509$, $N = 8$), although statistically non-significant, was also observed. With respect to the neuron-clinical correlation matrix (Fig. 10**B**), positive associations were found between Asyn_CSF and Abeta_CSF ($r = 0.95$, $p = 0.0003$, $N = 8$), N_ASyn and Asyn_CSF ($r = 0.97$, $p = 0.0317$, $N = 4$), UPDRS_TOT and UPDRS3 ($r = 0.85$, $p = 0.0069$, $n = 8$), UPDRSTOT_ON and UPDRS3 ($r = 0.85$, $p = 0.0068$,$N = 8$), UPDRS3_ON ($r = 0.74$, $p = 0.0345$, $N = 8$) and UPDRS_TOT ($r = 0.86$, $p = 0.0060$, $N = 8$), and N_THDiff and N_M_RESP ($r = 0.99$, $p = 0.0073$, $N = 4$). A negative association was detected between UPDRS3_ON and N_ASyn ($r = -0.98$, $p = 0.0176$, $N = 4$). A strong but non-significant association was also noted between N_ASyn Abeta_CSF ($r = 0.92$, $p = 0.084$, $N = 4$). In the fibroblast-neuron correlation matrix (Fig. 10**C)**, positive associations were detected between N_M_RESP and N_THDiff ($r = 0.99$, $p = 0.0073$, $N = 4$), F_DM and N_DM ($r = 1$, $p = 0.0190$, $N = 3$), F_B_RESP and N_OS ($r = 0.98$, $p = 0.0160$, $N = 4$) and F_M_RESP ($r = 0.94$, $p = 0.0004$, $N = 8$) and F_B_RESP, and N_VIABILITY and F_DM ($r = 0.96$, $p = 0.0432$, $N = 4$).

4. Discussion

In essence, we report parallel neurodegenerative phenotypes in sporadic PD fibroblasts and matched iPSC-based DA neurons, *derived*

Table 3
Statistical Analyses.

	Fibroblasts		Neurons						
Assay	β_F	SE_F	β_N	SE_N	β_F - β_N	t	df	p-value	
Viability	-0.1840	0.0501	-0.0491	0.1518	-0.1350	0.8445	8.5641	0.4214	
Oxidative Stress	0.3651	0.0901	0.2251	0.0389	0.1400	1.4263	20.8684	0.1686	
Mitochondrial Distortion	6.8750	1.0956	1.8990	0.2261	4.9760	4.4481	15.1415	0.0005	* **
Autophagic Vesicles	3.7426	0.6131	2.5874	0.5424	1.1552	1.4112	16.3849	0.1769	
Alpha Synuclein	0.8470	0.3994	1.5636	0.4134	-0.7166	1.2468	18.6029	0.2279	
Basal Respiration	0.4390	0.2130	-0.5926	0.2456	1.0316	3.1725	17.0028	0.0056	* *
Maximal Respiration	0.5843	0.2683	-0.5609	0.2801	1.1452	2.9521	18.4784	0.0084	* *
ATP	0.4170	0.2186	-0.5741	0.2308	0.9911	3.1170	18.3146	0.0059	* *
Proton Leak	0.6126	0.1854	-0.6705	0.3267	1.2831	3.4161	11.6700	0.0053	* *
Cell Size	-0.1870	0.0962	-0.3538	0.0430	0.1668	1.5826	21.1065	0.1284	
Morphological Differentiation	0.2532	0.0834	0.8110	0.0865	-0.5578	4.6409	18.9158	0.0002	* **

Welch-Satterthwaite's t-test on the difference of two slopes. β: slope of the regression line; SE: standard error of the slope; t: t statistic; df: degrees of freedom obtained following Satterthwaite (1946); F: fibroblast; N: neurons.
* $p < 0.05$; * * $p < 0.01$; * ** $p < 0.001$

from the same patient, which capture several fundamental PD features. Specifically, using this approach, we identified an array of pathological alterations in 'aged' PD patient fibroblasts and 'young' iPSC-derived DA neurons reprogrammed from the fibroblasts, that reflect disease processes relevant to both early neural development and ageing. Specific correlations between the fibroblast and neuronal features were seen which highlighted cell type- and tissue type-specific differences at play in PD. To our knowledge, this is the first time a bicameral patient-specific system consisting of both peripheral (skin fibroblast) and central/neural (iPSC-DAN) cells has been used to conduct a detailed modeling of idiopathic PD.

The study has a few important implications. Firstly, the data indicate that basic processes of PD can be expressed beyond the boundaries of the central nervous system, in peripheral cells such as skin fibroblasts – thus supporting the view of PD as a generalized metabolic disorder rather than a neuron-centric condition. Secondly, the corresponding changes in the DA neurons, derived from the fibroblasts, suggests that dysfunction in peripheral tissues would also be associated with abnormalities in the brains of respective sporadic PD patients. Thirdly, and in a broader sense, the results imply that by taking advantage of the reprogramming effect, different patient-derived cells, along the fibroblast-iPSC-neural progenitor-neuron-glia differentiation continuum, can be used as powerful models to identify cell type-specific neurodegenerative mechanisms active 'earlier' in the disease. By extension, utilization of these varied cell types can help build robust biomarker and drug testing platforms relevant to developing much needed early therapeutic interventions for PD.

In terms of the cellular phenotypes seen, in most cases, we found positive associations between data from similar fibroblast and neuronal assays. For instance, compared to their control counterparts, PD fibroblasts and PD iPSC-DAN showed reduced viability (MTT test), increased ROS levels (DCFH-DA test), abnormal mitochondrial structure (TEM) and function (Seahorse Mito Stress test), dysregulated autophagy (TEM and western blotting) and altered morphology (cell size and shape measurements). However, there were also notable differences. Interestingly, the pathological changes appeared to be more severe in the diseased fibroblasts than the iPSC-DAN, with greater differences seen between control and PD within this cell type. For instance, a greater reduction in viability and larger increases in oxidative stress, number of distorted mitochondria and autophagic vesicles were seen in PD fibroblasts vs PD iPSC-DAN when compared to their relevant controls. These changes could be attributed to the contribution of age-related variations in the fibroblasts; an aspect lost in the iPSC-DAN (Ivanov et al., 2016; Mertens et al., 2018). However, with respect to mitochondrial function, PD iPSC-DAN exhibited a worse phenotype than the fibroblasts. In particular, the PD iPSC-DAN had significantly lower basal and maximal respiration rates, proton leak, ATP production, and spare respiratory capacity compared to controls. The fibroblasts on the other hand showed higher basal and maximal respiration rates, proton leak, and spare respiratory capacity, and no significant changes in ATP production, compared to their controls. This occurred despite the elevations in the number of distorted mitochondria being higher in the fibroblasts compared to the neurons, suggesting that fibroblasts were able to compensate to some extent whereas the neurons were more vulnerable to the mitochondrial alterations. Also, although more distorted mitochondria were present in PD fibroblasts, the severity of the distortions (mitochondrial swelling, disruption of cristae, vacuolization, and mitophagy) were greater in PD iPSC-DAN than PD fibroblasts, supporting greater neuronal susceptibility to mitochondrial dysfunction. These data align with other studies that indicate that certain attributes of A9 midbrain DA neurons render them highly vulnerable to mitochondrial dysfunction (Greenamyre and Hastings, 2004; Matsuda et al., 2009; Sulzer, 2007; Surmeier et al., 2011).

It was also noted in the fibroblasts, that while there was increased proton leak and reduced coupling efficiency, the ATP production was not significantly different between control and PD groups. These data suggest that fibroblast PD mitochondria may have a higher capacity to generate the protonmotive force (PMF), which is the driving force for both OXPHOS and proton leak (Berry et al., 2018). High PMF is good for generating a robust ATP free energy, but it may also promote superoxide production. In support of this idea, higher ROS levels were seen in the PD fibroblasts compared to control cells. Also, by dissipating the PMF, the proton leak may protect against high free radical production. Thus, by increasing the proton leak, PD fibroblasts maybe "uncoupling to survive." In addition to these aspects, basal and maximal ECAR were significantly higher in the PD fibroblasts, in comparison to the iPSC PD-DAN, which showed opposite trends, indirectly pointing to different rates of glycolysis in the two cell types (although the OCR/ECAR ratios were not significantly different). All in all, these results support the notion that the fibroblasts are more able to compensate for mitochondrial impairments vs. the DA neurons.

The PD DA neurons also exhibited increased aSyn accumulation and altered electrophysiological profiles. Specifically, immunocytochemical and immmunoblotting data indicated that the PD iPSC-DAN generally expressed more aSyn and pSyn (pathological pSer129 epitope) than control neurons. Interestingly, aSyn expression appeared to be neuritic in controls cells whereas it was largely somatic in the PD neurons (Fig. 7). It is known that under normal conditions, aSyn is localized mainly to presynaptic terminals and axons of neurons (Oliveira et al., 2021). But, in the context of certain synucleinopathies, aSyn accumulates within the neuronal soma. Such aberrant localization of aSyn to sites proximal to the synapse suggests that impaired axonal transport maybe at play. Additionally, since basal autophagy was increased in the PD iPSC-DAN, and aSyn is a known autophagy cargo, these data imply that the PD neurons maybe engaging in more autophagic activity to plausibly cope with a higher load of aSyn. On the other hand, it is known that an increased aSyn protein burden may impair autophagy and reduce the efficiency of its degradation, via mechanisms such as Rab1a inhibition and blockade of the high-mobility group box 1 protein, thus generating a bidirectional positive feedback loop (Huang et al., 2017; Winslow et al., 2010). Thus, whether autophagy dysfunction alone suffices to increase aSyn or whether aSyn is the pathogenic driver, is an important question that needs to be studied.

Besides autophagy, it is recognized that aSyn aggregation can also negatively affect mitochondrial function, cytoskeletal structure and cell survival. In fact, it has been reported that aSyn can localize to mitochondria and induce severe ultrastructural deformation of the inner mitochondrial cristae membranes, massive swelling and a loss of respiratory function (Ganjam et al., 2019). There is also evidence that aSyn interacts with actin and tubulin, as well as their specific binding proteins, to impact cytoskeletal integrity (Carnwath et al., 2018; Oliveira da Silva and Liz, 2020). Cytoskeletal destabilization has been implicated as a major player that paves the way for neurodegeneration in PD, and our data on cell shape and size alterations in the PD neurons (as well as fibroblasts) suggest that such a mechanism could be at play in the human PD lines (McMurray, 2000; Pellegrini et al., 2017). Supporting this idea, a trend towards lower cell viability (MTT assay) was noted in the PD DA neurons compared to Controls. Interestingly, one of the PD lines showed higher viability compared to the all the others. This particular line originated from a younger (~55 yrs old) female subject with a short disease duration of 2.2 yrs. Also, the CSF ASyn levels (Table 1) and the number of cellular autophagic vesicles (Fig. 7) found in this subject were lower compared to the other three lines. It is possible that such factors may have contributed to higher resilience in these cells.

With respect to neuronal activity, a larger proportion of PD DA neurons were found to be inactive and did not show any action potentials, either spontaneously at rest or when induced with current steps, compared to controls. Moreover, although similar proportions of control and PD neurons were spontaneously active, a much smaller fraction of PD neurons could be induced to spike. Overall, these results implied that the PD iPSC-DAN were less electrically active as a population. Interestingly, it was also found that the control neurons had significantly more negative resting membrane potentials compared to the PD neurons, providing one reason why the control neurons were more readily activated. Neurons critically depend on mitochondrial function to establish membrane excitability and to execute the complex processes of neurotransmission and plasticity (Mattson et al., 2008). From this perspective, it is also possible that the impaired mitochondrial function/ATP production observed in the PD iPSC-DAN maybe contributing to their altered electrophysiological profiles.

The statistical correlational data comparing the fibroblast and neuronal outputs to different clinical measures from the patients, showed some interesting associations. For instance, a significant positive association between the number of autophagic vesicles and UPDRS scores was noted in the fibroblasts, and a significant negative association between population doubling time and UPDRS scores was seen. In neurons, significant positive relationships between cellular aSyn and patient CSF aSyn, and the efficiency of TH differentiation and maximal mitochondrial respiration rates were seen. However, it should be noted that the sample size for these correlations is small making interpretations difficult. Nevertheless, the presented analyses provide an appreciation of how such methods could support a robust stratification of the patient lines with respect to both cellular disease processes as well as clinical measures and creates a foundation for future investigations.

Essentially, the presented data establish specific patient fibroblast and iPSC-DAN phenotypes in the context of idiopathic PD. Nevertheless, further studies geared towards understanding the relationship of the observed fibroblast and DA neuron alterations to deeper mechanisms, will be needed. For instance, since iPSC-DAN mainly convey mechanisms of early neural vulnerabilities in PD, investigating aspects such as the influences of potential genetic variants would be important to study. Also, specific bioenergetic, biochemical and metabolic programs that may be contributing to the different phenotypic alterations would need to be investigated. Greater alpha-synuclein load can impact both mitochondria and autophagy and could be one important process linking the observed abnormalities in the PD cells. Our data, showing the presence of increased pathological pSer129 aggregates in PD vs control neurons, supports this idea. These important aspects will be explored in future work.

In conclusion, our identification of parallel phenotypes in sporadic PD fibroblast and iPSC-based DA neurons from the same patient, creates a unique system that can be used to study mechanisms relevant to both early neural and age-related peripheral influences driving PD progression. This system also provides a strong platform for the discovery of biomarkers for the early diagnosis and stratification of PD patients. Specifically, the study confirms the utility of patient skin fibroblasts as an accessible peripheral cell system reflective of disease status through the assay of multiple distinct biologic features. The study also reveals that iPSC-DAN reprogrammed and differentiated from the fibroblasts, can spontaneously express synchronous phenotypes, providing ‘early neural correlates’ of the fibroblast changes. To our knowledge, these findings, provide the first proof of principle that disease-relevant molecular and cellular phenotypes can be detected in easily obtainable tissues, such as skin fibroblasts, with demonstrated fidelity to underlying brain pathology. Thus, we propose that a multi-level modeling approach, involving different peripheral as well as central iPSC-derived neural cells, can enrich perspectives obtained from other important cellular systems, like directly reprogrammed cells, to support a deeper understanding of disease mechanisms and accelerate the development of rational therapeutics for early intervention in PD.

Declaration of Competing Interest

None.

Data Availability

Data will be made available on request.

Acknowledgements

We thank Dr Helena Morrison and Dr Wayne Willis for their expert input on the mitochondrial ATPIF1 and seahorse data. We also acknowledge Drs Tony Day and Paula Tonino for their assistance with the transmission electron microscopy work, which was performed in the Imaging Cores-Electron at the University of Arizona Research, Innovation, and Impact Core Facilities. The cell lines used in this study were partially obtained from the Parkinson’s Progression Markers Initiative (PPMI) [www.ppmi-info.org]. PPMI, a public private partnership, is funded by the Michael J. Fox Foundation for Parkinson’s Research and corporate sponsors [https://www.ppmi-info.org/about ppmi/who-we-are/study-sponsors]. The study was supported by a Michael J Fox Foundation Grant (MJFF 18366), Tech Launch Arizona (MDH-21), and UA intramural funds to LM, and National Eye Institute Grant R01-EY-026027 and NSF-1552184 to EE.

CRediT authorship contribution statement

MJC – Experimental design, Collection and assembly of data, Data analysis and Interpretation, Manuscript writing. AMJ – Collection and assembly of data, Data analysis and Interpretation, Manuscript writing. EC – Collection and assembly of data, Data analysis. TM – Collection, assembly and analysis of electrophysiology data, Manuscript writing. EE – Conception and design of electrophysiology experiments, Data analysis and resources support, Manuscript editing. KB – Collection, assembly, data analysis of ATPIF1 data, Manuscript editing. ML – Experimental design, execution, and data analysis support for Seahorse experiments. LJM – Experimental design, data interpretation and resources support for Seahorse experiments, Manuscript editing. SP – Statistical data analysis and interpretation, Manuscript editing. MSF– Statistical data analysis and interpretation, Manuscript editing. DB – Statistical data analysis and interpretation, Manuscript editing. LM – Overall conception and design of the study, Collection and assembly of data, Data analysis and Interpretation, Manuscript writing, Financial support, Final approval of manuscript.

Supporting information listing

1) Supplementary Figures 1, 2, 3 & 4.
2) Supplementary Methods.

Appendix A. Supporting information

Supplementary data associated with this article can be found in the online version at doi:10.1016/j.pneurobio.2023.102501.

References

Anandhan, A., Nguyen, N., Syal, A., Dreher, L.A., Dodson, M., Zhang, D.D., Madhavan, L., 2021. NRF2 loss accentuates parkinsonian pathology and behavioral dysfunction in human alpha-synuclein overexpressing mice. Aging Dis. 12, 964–982.

Arganda-Carreras, I., Fernandez-Gonzalez, R., Munoz-Barrutia, A., Ortiz-De-Solorzano, C., 2010. 3D reconstruction of histological sections: Application to mammary gland tissue. Microsc. Res Tech. 73, 1019–1029.

Auburger, G., Klinkenberg, M., Drost, J., Marcus, K., Morales-Gordo, B., Kunz, W.S., Brandt, U., Broccoli, V., Reichmann, H., Gispert, S., Jendrach, M., 2012. Primary skin fibroblasts as a model of Parkinson’s disease. Mol. Neurobiol. 46, 20–27.

Aversano, S., Caiazza, C., Caiazzo, M., 2022. Induced pluripotent stem cell-derived and directly reprogrammed neurons to study neurodegenerative diseases: the impact of aging signatures. Front Aging Neurosci. 14, 1069482.

Barker, R.A., Drouin-Ouellet, J., Parmar, M., 2015. Cell-based therapies for Parkinson disease-past insights and future potential. Nat. Rev. Neurol. 11, 492–503.

Berry, B.J., Trewin, A.J., Amitrano, A.M., Kim, M., Wojtovich, A.P., 2018. Use the protonmotive force: mitochondrial uncoupling and reactive oxygen species. J. Mol. Biol. 430, 3873–3891.

Bloem, B.R., Okun, M.S., Klein, C., 2021. Parkinson’s disease. Lancet 397, 2284–2303.

Carling, P.J., Mortiboys, H., Green, C., Mihaylov, S., Sandor, C., Schwartzentruber, A., Taylor, R., Wei, W., Hastings, C., Wong, S., Lo, C., Evetts, S., Clemmens, H., Wyles, M., Willcox, S., Payne, T., Hughes, R., Ferraiuolo, L., Webber, C., Hide, W., Wade-Martins, R., Talbot, K., Hu, M.T., Bandmann, O., 2020. Deep phenotyping of peripheral tissue facilitates mechanistic disease stratification in sporadic Parkinson's disease. Prog. Neurobiol. 187, 101772.

Carnwath, T., Mohammed, R., Tsiang, D., 2018. The direct and indirect effects of alpha-synuclein on microtubule stability in the pathogenesis of Parkinson's disease. Neuropsychiatr. Dis. Treat. 14, 1685–1695.

Chambers, S.M., Fasano, C.A., Papapetrou, E.P., Tomishima, M., Sadelain, M., Studer, L., 2009. Highly efficient neural conversion of human ES and iPS cells by dual inhibition of SMAD signaling. Nat. Biotechnol. 27, 275–280.

Dorsey, E.R., Sherer, T., Okun, M.S., Bloem, B.R., 2018. The emerging evidence of the Parkinson pandemic. J. Park. Dis. 8, S3–S8.

Galvagnion, C., Marlet, F.R., Cerri, S., Schapira, A.H.V., Blandini, F., Di Monte, D.A., 2022. Sphingolipid changes in Parkinson L444P GBA mutation fibroblasts promote alpha-synuclein aggregation. Brain 145, 1038–1051.

Ganjam, G.K., Bolte, K., Matschke, L.A., Neitemeier, S., Dolga, A.M., Hollerhage, M., Hoglinger, G.U., Adamczyk, A., Decher, N., Oertel, W.H., Culmsee, C., 2019. Mitochondrial damage by alpha-synuclein causes cell death in human dopaminergic neurons. Cell Death Dis. 10, 865.

Gonzalez-Casacuberta, I., Juarez-Flores, D.L., Ezquerra, M., Fucho, R., Catalan-Garcia, M., Guitart-Mampel, M., Tobias, E., Garcia-Ruiz, C., Fernandez-Checa, J.C., Tolosa, E., Marti, M.J., Grau, J.M., Fernandez-Santiago, R., Cardellach, F., Moren, C., Garrabou, G., 2019. Mitochondrial and autophagic alterations in skin fibroblasts from Parkinson disease patients with Parkin mutations. Aging (Albany NY) 11, 3750–3767.

Greenamyre, J.T., Hastings, T.G., 2004. Biomedicine. Parkinson's–divergent causes, convergent mechanisms. *Science* 304, 1120–1122.

Gu, X., Ma, Y., Liu, Y., Wan, Q., 2021. Measurement of mitochondrial respiration in adherent cells by Seahorse XF96 Cell Mito Stress Test. STAR Protoc. 2, 100245.

Huang, J., Yang, J., Shen, Y., Jiang, H., Han, C., Zhang, G., Liu, L., Xu, X., Li, J., Lin, Z., Xiong, N., Zhang, Z., Xiong, J., Wang, T., 2017. HMGB1 Mediates autophagy dysfunction via perturbing Beclin1-Vps34 complex in dopaminergic cell model. Front. Mol. Neurosci. 10, 13.

Ivanov, N.A., Tao, R., Chenoweth, J.G., Brandtjen, A., Mighdoll, M.I., Genova, J.D., McKay, R.D., Jia, Y., Weinberger, D.R., Kleinman, J.E., Hyde, T.M., Jaffe, A.E., 2016. Strong components of epigenetic memory in cultured human fibroblasts related to site of origin and donor age. PLoS Genet. 12, e1005819.

Johnson, M.E., Stecher, B., Labrie, V., Brundin, L., Brundin, P., 2019. Triggers, Facilitators, And Aggravators: Redefining Parkinson's Disease Pathogenesis. Trends Neurosci. 42, 4–13.

Kriks, S., Shim, J.W., Piao, J., Ganat, Y.M., Wakeman, D.R., Xie, Z., Carrillo-Reid, L., Auyeung, G., Antonacci, C., Buch, A., Yang, L., Beal, M.F., Surmeier, D.J., Kordower, J.H., Tabar, V., Studer, L., 2011. Dopamine neurons derived from human ES cells efficiently engraft in animal models of Parkinson's disease. Nature 480, 547–551.

Kumar, P., Nagarajan, A., Uchil, P.D., 2018. Analysis of cell viability by the MTT assay. Cold Spring Harb. Protoc. 2018.

Kutner, M.H., Nachtsheim, C.J., Neter, J., 2004. Applied Linear Regression Models, 4th Edition. McGraw-Hill Irwin.

Lim, S.Y., Fox, S.H., Lang, A.E., 2009. Overview of the extranigral aspects of Parkinson disease. Arch. Neurol. 66, 167–172.

Malkus, K.A., Tsika, E., Ischiropoulos, H., 2009. Oxidative modifications, mitochondrial dysfunction, and impaired protein degradation in Parkinson's disease: how neurons are lost in the Bermuda triangle. Mol. Neurodegener. 4, 24.

Matsuda, W., Furuta, T., Nakamura, K.C., Hioki, H., Fujiyama, F., Arai, R., Kaneko, T., 2009. Single nigrostriatal dopaminergic neurons form widely spread and highly dense axonal arborizations in the neostriatum. J. Neurosci. 29, 444–453.

Mattson, M.P., Gleichmann, M., Cheng, A., 2008. Mitochondria in neuroplasticity and neurological disorders. Neuron 60, 748–766.

McMurray, C.T., 2000. Neurodegeneration: diseases of the cytoskeleton? Cell Death Differ. 7, 861–865.

Mertens, J., Reid, D., Lau, S., Kim, Y., Gage, F.H., 2018. Aging in a dish: iPSC-derived and directly induced neurons for studying brain aging and age-related neurodegenerative diseases. Annu. Rev. Genet. 52, 271–293.

Mortiboys, H., Thomas, K.J., Koopman, W.J., Klaffke, S., Abou-Sleiman, P., Olpin, S., Wood, N.W., Willems, P.H., Smeitink, J.A., Cookson, M.R., Bandmann, O., 2008. Mitochondrial function and morphology are impaired in parkin-mutant fibroblasts. Ann. Neurol. 64, 555–565.

Murphy, M.P., 2009. How mitochondria produce reactive oxygen species. Biochem. J. 417, 1–13.

Oliveira, L.M.A., Gasser, T., Edwards, R., Zweckstetter, M., Melki, R., Stefanis, L., Lashuel, H.A., Sulzer, D., Vekrellis, K., Halliday, G.M., Tomlinson, J.J., Schlossmacher, M., Jensen, P.H., Schulze-Hentrich, J., Riess, O., Hirst, W.D., El-Agnaf, O., Mollenhauer, B., Lansbury, P., Outeiro, T.F., 2021. Alpha-synuclein research: defining strategic moves in the battle against Parkinson's disease. NPJ Park. Dis. 7, 65.

Oliveira da Silva, M.I., Liz, M.A., 2020. Linking alpha-synuclein to the actin cytoskeleton: consequences to neuronal function. Front. Cell Dev. Biol. 8, 787.

Oyama, Y., Hayashi, A., Ueha, T., Maekawa, K., 1994. Characterization of 2',7'-dichlorofluorescin fluorescence in dissociated mammalian brain neurons: estimation on intracellular content of hydrogen peroxide. Brain Res. 635, 113–117.

Pellegrini, L., Wetzel, A., Granno, S., Heaton, G., Harvey, K., 2017. Back to the tubule: microtubule dynamics in Parkinson's disease. Cell. Mol. Life Sci. 74, 409–434.

Poewe, W., 2010. Parkinson disease: treatment of the nonmotor symptoms of Parkinson disease. Nat. Rev. Neurol. 6, 417–418.

Poewe, W., Seppi, K., Tanner, C.M., Halliday, G.M., Brundin, P., Volkmann, J., Schrag, A. E., Lang, A.E., 2017. Parkinson disease. Nat. Rev. Dis. Prim. 3, 17013.

R Core Team (2021). R: A language and environment for statistical computing. R Foundation for Statistical Computing, Vienna, Austria. URL: https://www.R-project.org/.

Satterthwaite, F.E., 1946. An approximate distribution of estimates of variance components. Biometrics Bull. 2 (6), 110–114.

Shannon, K.M., 2007. Dopamine: so "last century". Neurology 69, 329–330.

Sulzer, D., 2007. Multiple hit hypotheses for dopamine neuron loss in Parkinson's disease. Trends Neurosci. 30, 244–250.

Surmeier, D.J., Guzman, J.N., Sanchez-Padilla, J., Goldberg, J.A., 2011. The origins of oxidant stress in Parkinson's disease and therapeutic strategies. Antioxid. Redox Signal 14, 1289–1301.

Teves, J.M.Y., Bhargava, V., Kirwan, K.R., Corenblum, M.J., Justiniano, R., Wondrak, G. T., Anandhan, A., Flores, A.J., Schipper, D.A., Khalpey, Z., Sligh, J.E., Curiel-Lewandrowski, C., Sherman, S.J., Madhavan, L., 2017. Parkinson's disease skin fibroblasts display signature alterations in growth, redox homeostasis, mitochondrial function, and autophagy. Front Neurosci. 11, 737.

Tolosa, E., Garrido, A., Scholz, S.W., Poewe, W., 2021. Challenges in the diagnosis of Parkinson's disease. Lancet Neurol. 20, 385–397.

Venditti, P., Di Stefano, L., Di Meo, S., 2013. Mitochondrial metabolism of reactive oxygen species. Mitochondrion 13, 71–82.

Wei T, Simko V (2021). R package 'corrplot': Visualization of a Correlation Matrix. (Version 0.92), .

Welch, B.L., 1947. The generalization of "Student's" problem when several different population variances are involved. Biometrika 34 (1/2), 28–35.

Wickham, H., 2016. ggplot2: Elegant Graphics for Data Analysis. Springer-Verlag New York. https://ggplot2.tidyverse.org.

Winslow, A.R., Chen, C.W., Corrochano, S., Acevedo-Arozena, A., Gordon, D.E., Peden, A.A., Lichtenberg, M., Menzies, F.M., Ravikumar, B., Imarisio, S., Brown, S., O'Kane, C.J., Rubinsztein, D.C., 2010. alpha-Synuclein impairs macroautophagy: implications for Parkinson's disease. J. Cell Biol. 190, 1023–1037.

Young, K., Morrison, H., 2018. Quantifying microglia morphology from photomicrographs of immunohistochemistry prepared tissue using imageJ. J. Vis. Exp.